Attitude Dynamics of Small Magnetic Axisymmetric Satellites in Near-Equatorial LEO/VLEO

Dmitry A. Sizov*
Nazarbayev University, Astana, 010000, Kazakhstan

Vladimir S. Aslanov†
Moscow Aviation Institute (National Research University), Moscow, 125993, Russia

This study deals with the attitude motion of small magnetic axisymmetric satellites in near-equatorial circular LEO/VLEO subjected to the joint action of the environmental torques, namely, aerodynamic, gravitational, and magnetic. It is shown that if the satellite has only a longitudinal component of the intrinsic magnetic moment, it is convenient to separate the attitude motion into the unperturbed motion and the perturbations from the non-potential components of the considered torques. The bifurcation analysis of the critical points of the unperturbed dynamic potential demonstrates the influence of the main system parameters on their existence and stability and provides an intuitive understanding of the possible regimes of attitude motion. Numerical simulations show that, in addition to regular attitude motion of the considered satellites, chaotic regimes are also possible.

Nomenclature

A	=	longitudinal moment of inertia, kg·m^2
A_r	=	reference area, m^2
$\boldsymbol{B}$	=	Earth magnetic field, tesla
C	=	transverse moment of inertia, kg·m^2
h	=	orbital altitude, m
H	=	Hamiltonian, J
$\mathcal{H}$	=	Hessian matrix
i	=	orbital inclination, rad
J	=	moment of inertia matrix
$\boldsymbol{k}_e$	=	unit vector in the direction of the Earth's magnetic field dipole
L	=	Lagrangian, J

*Instructor, Department of Mechanical and Aerospace Engineering, 53, Kabanbay Batyr Avenue
†Professor, Mechatronics and Theoretical Mechanics Department, 4, Volokolamskoye Shosse

L_r = reference length, m

$\boldsymbol{M}_G$ = gravitational torque, N·m

$\boldsymbol{M}_d$ = damping aerodynamic torque, N·m

$\boldsymbol{M}_M$ = magnetic torque, N·m

$\boldsymbol{M}_C$ = conservative component of the magnetic torque, N·m

$\boldsymbol{M}_{NC}$ = non-conservative component of the magnetic torque, N·m

M_θ = restoring aerodynamic torque, N·m

$\bar{M}_\theta$ = restoring aerodynamic torque coefficient

$\bar{M}_k^{\omega_k}$ = damping aerodynamic torque coefficients

p_ϕ = generalized impulse corresponding to spin angle, N·m·s

Q_k = generalized forces, N·m

$\bar{Q}_k$ = dimensionless generalized forces

R = Routhian, J

R_0 = orbital radius, m

R_e = mean radius of the Earth, m

T = kinetic energy of the satellite, J

U = dynamic potential, J

$\bar{U}$ = dimensionless dynamic potential

$\boldsymbol{V}$ = velocity vector of the center of mass of the satellite, m/s

V = potential energy of the satellite, J

V_A = restoring aerodynamic torque potential, J

V_G = gravitational torque potential, J

V_M = magnetic torque potential, J

α = dimensionless parameter characterizing the magnitude of the restoring aerodynamic torque

β = dimensionless parameter characterizing joint action of the magnetic and gyroscopic torques

γ = dimensionless parameter characterizing the magnitude of the gravitational torque

δ = dimensionless parameter characterizing the magnitude of the damping aerodynamic torque

ε = dimensionless perturbation parameter

θ = angle of attack, rad

μ_G = gravitational parameter of the Earth, $m^3 \cdot s^{-2}$

$\boldsymbol{\mu}$ = intrinsic magnetic moment of the satellite, $A \cdot m^2$

μ_m = geomagnetic dipole moment, $A \cdot m^2$

μ_0 = magnetic permeability of vacuum, N/A^2

ν = true anomaly, rad

ρ = density of the atmosphere, kg/m^3

φ = spin angle, rad

ψ = precession angle, rad

ω = absolute angular speed, rad/s

Ω = orbital angular speed, rad/s

Subscripts and Supersripts

B = expressed in the Body-fixed frame

O = expressed in the Orbital frame

crit = critical

I. Introduction

Near-equatorial orbits offer certain advantages for satellites. Specifically, such orbits are useful for satellites aimed to provide information about tropical weather processes [1]. Near-equatorial orbits offer other advantages, such as for communications: a satellite in such an orbit is able to pass over an equatorial communication center on each rotation [2], as opposed to the varying ground track of satellites placed in inclined orbits. It should also be noted that the Earth's magnetic field near the equator has a varying in-plane component depending on the satellite location, which makes magnetic attitude control complicated, but still feasible [3, 4].

Although most near-equatorial satellites are in geostationary orbit with zero inclination and an orbital radius of 42,164 km, a significant fraction of them orbit the Earth at much lower altitudes (less than 700 km). To study the attitude motion at these altitudes, in addition to the gravity-gradient and magnetic torques, one must consider the interaction with the atmosphere [5–12]. This interaction generates the aerodynamic torque, which is a considerable resource for angular stabilization [13–19]. The focus on aerodynamic stabilization arises from the observation that as a satellite's size decreases, the impact of aerodynamic torques on its angular motion becomes more pronounced, which follows from a simple scaling analysis. Specifically, the aerodynamic torque scales with the cube of the characteristic length of the satellite, whereas the satellite's moment of inertia scales with the fifth power of this length. Consequently, as the satellite becomes smaller, its moment of inertia decreases at a faster rate compared to the aerodynamic torque. This results in an increase in angular acceleration induced by the aerodynamic torque. Currently, with the growing attention to very low Earth orbits (VLEO) [20–23], the aerodynamic stabilization by means of deployable tail panels [24–26] or aeroshells [27–29] has become one of the popular trends in today's design of small satellites.

Deployable elements are characterized by a relatively high risk of uneven deployment. In the case of tail panels, such a deployment may result in undesirable satellite pointing and considerable high-frequency vibrations [30]. A recent in-orbit test [27] of a deployable aeroshell revealed another negative consequence of uneven deployment: aerodynamically stabilized satellites may undesirably spin due to unexpected distortion of the aeroshell. The combined action of the environmental torques and gyroscopic torque resulting from such spinning can produce multiple torque equilibrium attitudes. The pioneering works on these equilibrium positions [15, 16] considered only conservative environmental torques, such as gravitational and restoring aerodynamic torque. In more recent studies, additional torques, such as inertial torques due to elastic elements [31, 32], magnetic torques [33–36], damping aerodynamic torques [32, 35–37], are taken into account. Most of these works demonstrate that, under certain circumstances, the satellite may pass from regular attitude motion into chaotic regimes. One possible way to facilitate studying chaos in the attitude motion is to use the concepts of unperturbed motion, caused by large torques, and perturbed motion, where perturbations due to much smaller torques are also considered. If all the torques causing the unperturbed motion are conservative, i.e., have potential functions depending on the satellite's attitude, the investigation can be substantially facilitated by the use of the Lagrangian or Hamiltonian approach. In this case, such concepts as dynamic potential and integrals of motion play an important role. Previous works discuss the integrals of the attitude motion of satellites in the presence of a magnetic torque only [38], in the cases of the joint action of the aerodynamic and gravitational torques [14, 15], or magnetic and gravitational torques [39].

The present study is aimed to develop a framework for analyzing regular and chaotic regimes of the attitude motion of spinning small axisymmetric magnetic satellites in near-equatorial LEO/VLEO, exploiting the effect of small orbital inclination on the magnetic torque and taking into consideration the aerodynamic damping. The novelty of the article is that it is shown that the integrals of the unperturbed attitude motion of a passive near-equatorial satellite contain terms coming from three torques: aerodynamic, gravitational, and magnetic. The use of these integrals for derivation of the dynamic potential with the subsequent detailed analysis of its critical points is another novel aspect of the paper. Moreover, new numerical results and visualizations are obtained for the attitude motion of a typical passive aerodynamically stabilized satellite which show that, at a certain level of perturbations, its attitude motion can be chaotic.

The structure of the paper is the following. In Section II, the chosen method of describing the motion is discussed, and all formulas necessary for modeling the environmental torques are given. Section III is dedicated to the derivation of the equations of attitude motion. Particular attention is paid to the investigation of the dynamic potential of the unperturbed motion and the critical points of this potential. In Section IV, the attitude motion of an aerodynamically stabilized satellite is discussed, the bifurcation analysis of critical points is carried out, and the numerical simulations are performed, demonstrating the chaotic character of the motion. Finally, in Conclusion, the results are summarized and analyzed.

II. Problem Statement

This paper deals with the attitude motion of a particular class of passive aerodynamically stabilized satellites in LEO/VLEO. Before developing the mathematical model of the attitude motion, we will first formulate the key assumptions, then introduce the reference frames used, and finally discuss the conservative and non-conservative environmental torques considered.

A. Key Assumptions

1) The satellite's orbit is circular and has a small inclination.
2) The satellite is axisymmetric and has a diagonal inertia tensor:

$$J = \begin{pmatrix} A & 0 & 0 \\ 0 & C & 0 \\ 0 & 0 & C \end{pmatrix} \tag{1}$$

where A and C are respectively the longitudinal and transverse moments of inertia.
3) The vector of the satellite's intrinsic magnetic moment lies on its longitudinal axis.
4) The Earth's magnetic field is equivalent to that of a dipole placed in the center of the planet and aligned with its axis of rotation.
5) The non-conservative torques are small compared to the conservative ones.

B. Reference Frames and Euler angles

In this study, three main reference frames are used.

1) The inertial geocentric equatorial frame E (Fig. 1) is defined through a set $\hat{\boldsymbol{e}}_k$, $k = 1, 2, 3$, with the origin at the center of mass of the Earth. The vectors $\hat{\boldsymbol{e}}_1$ and $\hat{\boldsymbol{e}}_2$ lie in the equatorial plane, the vector $\hat{\boldsymbol{e}}_1$ passes through the ascending node of the satellite's orbit and thus coincides with the node line, and the vector $\hat{\boldsymbol{e}}_3$ is aligned with the Earth's rotation axis.
2) The orbital frame O (Fig. 1 and 2) is defined through a set $\hat{\boldsymbol{o}}_k$ based at the satellite's center of mass (CoM), the latter moving along the orbit with a velocity $\boldsymbol{V}$. The position of the CoM in the orbit is defined by the mean anomaly ν measured from the perigee, which, for circular orbits, can be chosen arbitrarily [40] and, in this study, coincides with the ascending node. The $\hat{\boldsymbol{o}}_1$ vector is in the direction of the velocity $\boldsymbol{V}$, the $\hat{\boldsymbol{o}}_3$ vector is directed along the radius vector of the CoM. Both of these vectors lie in the orbital plane, inclined at an angle i with respect to the equatorial plane. For any vector $\boldsymbol{v}$, the coordinate transformation between the orbital and the

inertial geocentric equatorial frames can be performed as follows

$$\boldsymbol{v}^E = \Phi \boldsymbol{v}^O \tag{2}$$

where

$$\Phi = \begin{pmatrix} -\sin\nu & 0 & \cos\nu \\ \cos i \cos\nu & -\sin i & \cos i \sin\nu \\ \cos\nu \sin i & \cos i & \sin i \sin\nu \end{pmatrix}. \tag{3}$$

3) The body-fixed frame B (Fig. 2) is defined through a set of unit vectors $\hat{\boldsymbol{b}}_k$, the $\hat{\boldsymbol{b}}_1$ vector lying along the axis of symmetry, and $\hat{\boldsymbol{b}}_2$ and $\hat{\boldsymbol{b}}_3$ aligned with the satellite's transverse principal axes. The attitude of the satellite is determined using a $(1, 3, 1)$ set of Euler angles (ψ, θ, φ), describing the orientation of the body-fixed frame relative to the orbital frame. The coordinate transformation between these frames can be performed as follows:

$$\boldsymbol{v}^B = \Theta \boldsymbol{v}^O \tag{4}$$

where

$$\Theta = \begin{pmatrix} \cos\theta & \cos\psi\sin\theta & \sin\theta\sin\psi \\ -\cos\varphi\sin\theta & \cos\theta\cos\varphi\cos\psi - \sin\varphi\sin\psi & \cos\psi\sin\varphi + \cos\theta\cos\varphi\sin\psi \\ \sin\theta\sin\varphi & -\cos\theta\cos\psi\sin\varphi - \cos\varphi\sin\psi & \cos\varphi\cos\psi - \cos\theta\sin\varphi\sin\psi \end{pmatrix}, \tag{5}$$

ψ is the precession angle, $-\infty < \psi < \infty$; θ is the angle of attack, $0 < \theta < \pi$; φ is the spin angle, $-\infty < \varphi < \infty$.

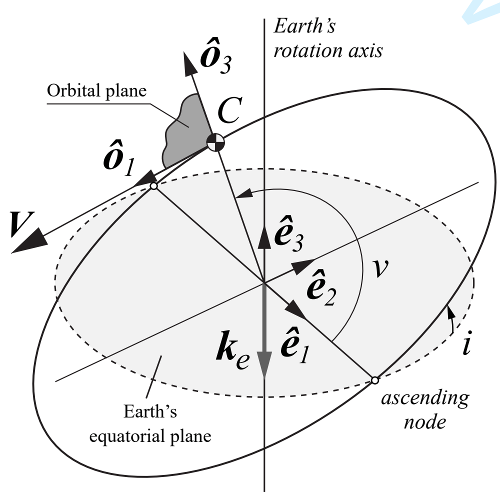

Fig. 1 Inertial geocentric equatorial and orbital frames.

Two auxiliary intermediate coordinate frames I and I' are defined through unit vector sets $\hat{\boldsymbol{i}}_k$, $\hat{\boldsymbol{i}}'_k$, respectively (Fig. 2). The orientations of these frames relative to the orbital frame are determined by the above-mentioned rotations: a single rotation by the angle ψ for the $\hat{\boldsymbol{i}}_k$ frame and two successive rotations by the angles ψ and θ for the $\hat{\boldsymbol{i}}'_k$ frame.

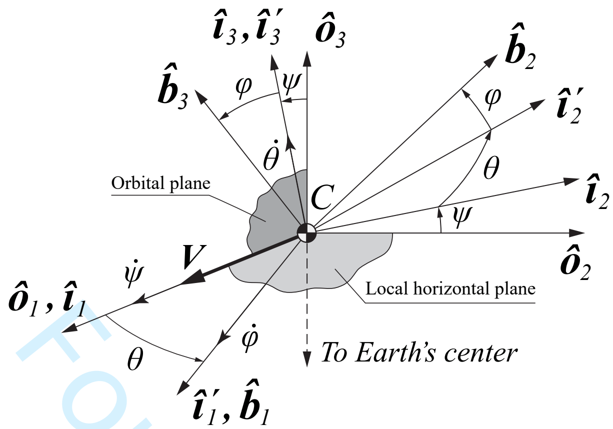

Fig. 2 Orbital and body-fixed frames. Euler angles.

Let us note that, clearly, the use of Euler angles is not the only way to determine the attitude motion. There are plenty of alternatives, having their advantages, e.g., quaternions do not suffer from singularities when defining rigid body orientation, while action-angle variables provide a simpler derivation of the integrals of motion. However, the present paper uses Euler angles because the dynamic potential (see Section III.A.2), which is of great importance for an intuitive understanding of the satellite attitude motion under consideration, is best visualized using Euler angles (see Section IV.C).

C. Environmental Torques

1. Gravitational Torque

The gravitational torque is defined as [14]

$$\boldsymbol{M}_G = 3\Omega^2 \left(\hat{\boldsymbol{o}}_3 \times J\hat{\boldsymbol{o}}_3\right) \tag{6}$$

where $\Omega = \sqrt{\mu_G / R_0^3}$ is the orbital angular speed, $R_0 = R_e + h$ is the orbit radius, h is the altitude, R_e is the mean radius of the Earth, and μ_G is its gravitational parameter. The gravitational torque is well known to be conservative, and, in terms of the chosen Euler angles, its potential energy can be expressed as

$$V_G = -\frac{3}{2}\left(C - A\right)\Omega^2 \sin^2\theta \sin^2\psi. \tag{7}$$

2. Restoring Aerodynamic Torque

For axisymmetric satellites, the restoring aerodynamic torque acts about the nutation axis determined by the unit vector $\hat{\boldsymbol{i}}_3$ (Fig. 2). This torque is defined as [16]:

$$M_\theta = c_r \bar{M}_\theta \tag{8}$$

where

$$c_r = \frac{\rho V^2}{2} A_r L_r, \tag{9}$$

L_r is the reference length, A_r is the reference area, $V = \Omega R_0$ is the orbital speed of the CoM, ρ is the density of the atmosphere calculated in this study using the Jacchia-Bowman 2008 model [41] for mean solar and geomagnetic activities , $\bar{M}_\theta$ is the restoring aerodynamic torque coefficient, either obtained experimentally or approximately calculated analytically, and typically expressed as a Fourier series with coefficients b_j :

$$\bar{M}_\theta = \sum_{j=1}^{n} b_j \sin j\theta \tag{10}$$

where n is the number of harmonics. The potential function of the restoring aerodynamic torque is

$$V_A = -\int_0^\theta M_\theta d\theta = c_r \sum_{j=1}^{n} \frac{1}{j} b_j \cos j\theta. \tag{11}$$

3. Damping Aerodynamic Torque

In VLEO, the effect of the aerodynamic damping torque [42] is significant, so it is taken into account in the present study. The damping torque can be written as

$$\boldsymbol{M}_d = c_d \begin{pmatrix} \bar{M}_1^{\omega_1} \omega_1 \\ \bar{M}_2^{\omega_2} \omega_2 \\ \bar{M}_3^{\omega_3} \omega_3 \end{pmatrix}^B \tag{12}$$

where the superscript B indicates that the vector is expressed in the body-fixed frame [43],

$$c_d = \frac{\rho V}{2} A_r L_r^2, \tag{13}$$

ω_k are the components of the angular velocity vector $\boldsymbol{\omega}$,

$$\boldsymbol{\omega} = \begin{pmatrix} \omega_1 \\ \omega_2 \\ \omega_3 \end{pmatrix} = \begin{pmatrix} \dot{\varphi} + \dot{\psi}\cos\theta + \Omega\cos\psi\sin\theta \\ \dot{\theta}\sin\varphi - \dot{\psi}\cos\varphi\sin\theta + \Omega\left(\cos\theta\cos\varphi\cos\psi - \sin\varphi\sin\psi\right) \\ \dot{\theta}\cos\varphi + \dot{\psi}\sin\theta\sin\varphi - \Omega\left(\cos\theta\cos\psi\sin\varphi + \sin\psi\cos\varphi\right) \end{pmatrix}^B, \tag{14}$$

expressed in the B frame (Fig. 2), and $\bar{M}_k^{\omega_k}$ are the coefficients of the damping torque:

$$\begin{aligned} \bar{M}_1^{\omega_1}(\theta,\varphi) &= \sum_{i=0}^{p}\sum_{j=0}^{r} a_{1,i,j}\cos i\theta\cos j\varphi, \\ \bar{M}_2^{\omega_2}(\theta,\varphi) &= \sum_{i=0}^{p}\sum_{j=0}^{r} a_{2,i,j}\cos i\theta\cos j\varphi, \\ \bar{M}_3^{\omega_3}(\theta,\varphi) &= \sum_{i=0}^{p}\sum_{j=0}^{r} a_{2,i,j}\cos i\theta\cos j(\varphi+\pi/2) \\ &= \bar{M}_2^{\omega_2}(\theta,\varphi+\pi/2) \end{aligned} \tag{15}$$

where $a_{1,i,j}$ and $a_{2,i,j}$ are 2D Fourier series coefficients, p, r are the numbers of harmonics. Clearly, the damping aerodynamic torque is not conservative, as it is a function of the angular velocity components, by virtue of Eq. (12).

4. Magnetic Torque

The well-known expression for the magnetic torque is [5]

$$\boldsymbol{M}_M = \boldsymbol{\mu} \times \boldsymbol{B} \tag{16}$$

where $\boldsymbol{\mu}$ is the intrinsic magnetic moment. For an axisymmetric magnetic satellite,

$$\boldsymbol{\mu} = \begin{pmatrix} M \\ 0 \\ 0 \end{pmatrix}^B, \tag{17}$$

where M is the longitudinal component of the intrinsic magnetic moment, $\boldsymbol{B}$ is the magnetic field of the Earth,

$$\boldsymbol{B} = \frac{\mu_0\mu_m}{4\pi R_0^3}\boldsymbol{B}_0, \tag{18}$$

where μ_m is the geomagnetic dipole moment, μ_0 is the magnetic permeability of vacuum, $\boldsymbol{B}_0$ is a vector defined as [44]

$$\boldsymbol{B}_0 = 3\hat{\boldsymbol{o}}_3 \left(\boldsymbol{k}_e \cdot \hat{\boldsymbol{o}}_3\right) - \boldsymbol{k}_e \tag{19}$$

where $\boldsymbol{k}_e$ is a unit vector in the direction of the dipole modeling the Earth's magnetic field (Fig. 1). Expressed in the orbital frame, the vector $\boldsymbol{B}_0$ has the form

$$\boldsymbol{B}_0 = \begin{pmatrix} \cos\nu \sin i \\ \cos i \\ -2\sin i \sin\nu \end{pmatrix}^O \tag{20}$$

where ν is the true anomaly,

$$\nu = \Omega t, \tag{21}$$

which will be used as the dimensionless time, and i is the orbital inclination. Since the inclination of near-equatorial orbits is small, let us simplify the vector $\boldsymbol{B}_0$ using the small angle approximation:

$$\boldsymbol{B}_0 \approx \begin{pmatrix} i\cos\nu \\ 1 \\ -2i\sin\nu \end{pmatrix}^O. \tag{22}$$

With Eqs. (17), (18), and (22) taken into account, the magnetic torque Eq. (16) for near-equatorial orbits can be thus approximately written as a sum of two components:

$$\boldsymbol{M}_M = \boldsymbol{M}_C + i\boldsymbol{M}_{NC}. \tag{23}$$

The first component of the magnetic torque $\boldsymbol{M}_C$,

$$\boldsymbol{M}_C = \mathcal{M}\begin{pmatrix} 0 \\ \cos\theta\sin\varphi\cos\psi + \cos\varphi\sin\psi \\ \cos\theta\cos\varphi\cos\psi - \sin\varphi\sin\psi \end{pmatrix}^B, \tag{24}$$

is conservative and has a potential function

$$V_{MC} = -\mathcal{M}\sin\theta\cos\psi \tag{25}$$

where

$$\mathcal{M} = \frac{M\mu_0\mu_m}{4\pi R_0^3} \tag{26}$$

is a constant factor. The second component of the magnetic torque $i\boldsymbol{M}_{NC}$ is not conservative, since $\boldsymbol{M}_{NC}$ is a function of the true anomaly:

$$\boldsymbol{M}_{NC}(\nu) = \mathcal{M}\begin{pmatrix} 0 \\ 2\cos\varphi\cos\psi\sin\nu - (2\cos\theta\sin\psi\sin\nu + \sin\theta\cos\nu)\sin\varphi \\ -2(\cos\theta\cos\varphi\sin\psi + \sin\varphi\cos\psi)\sin\nu + \sin\theta\cos\varphi\cos\nu \end{pmatrix}^B. \tag{27}$$

III. Mathematical Model of Attitude Motion of an Axisymmetric Magnetic Satellite

Since most of the torques considered in this study are conservative, it is convenient to write the equations of motion in the Lagrangian form using the Euler angles (see Section II.B) as generalized coordinates q_k, $k = 1, 2, 3$:

$$q_1 = \theta, \quad q_2 = \psi, \quad q_3 = \varphi. \tag{28}$$

The kinetic energy is

$$T = \frac{1}{2}\left(A{\omega_1}^2 + C({\omega_2}^2 + {\omega_3}^2)\right), \tag{29}$$

and, after substitution of Eq. (14), it can be written as

$$T = \frac{1}{2}A\left[\dot\varphi + \dot\psi\cos\theta + \Omega\cos\psi\sin\theta\right]^2 + \frac{1}{2}C\left[\dot\theta^2 + \left(\Omega\cos\theta\cos\psi - \dot\psi\sin\theta\right)^2 - 2\Omega\dot\theta\sin\psi + \Omega^2\sin^2\psi\right]. \tag{30}$$

The potential energy is

$$V = V_G + V_A + V_{MC} \tag{31}$$

where V_G, V_A, and V_{MC} are defined by Eqs. (7), (11), and (25), respectively. Using Eqs. (30) and (31), one can obtain the Lagrangian as

$$\begin{aligned} L &= T - V = \\ &= \frac{1}{2}A\left[\dot\varphi + \dot\psi\cos\theta + \Omega\cos\psi\sin\theta\right]^2 + \frac{1}{2}C\left[\dot\theta^2 + \left(\Omega\cos\theta\cos\psi - \dot\psi\sin\theta\right)^2 - 2\Omega\dot\theta\sin\psi + \Omega^2\sin^2\psi\right] \\ &+ \frac{3}{2}(C - A)\,\Omega^2\sin^2\theta\sin^2\psi - c_r\sum_{j=1}^{n}\frac{1}{j}b_j\cos j\theta + \mathcal{M}\sin\theta\cos\psi. \end{aligned} \tag{32}$$

Note that the generalized coordinate φ does not appear in the Lagrangian (32). In the case of conservative torques, one can reduce the number of degrees of freedom using Routh's procedure [45], and the attitude motion of the satellite can be described simply as the motion of its longitudinal axis.

In order to take advantage of these benefits, in this study, the attitude motion will be split into the unperturbed part and perturbations. The non-conservative torques acting on the satellite are the damping aerodynamic torque $\boldsymbol{M}_d$ [Eq. (12)] and the part of magnetic torque $i\boldsymbol{M}_{NC}$ (see (27)); compared to the other torques acting on the satellite, both of these torques are small, so it is convenient to consider them as perturbations. Then the satellite's motion under the conservative torques can be called unperturbed. Accordingly, the perturbed motion is the attitude motion of the satellite subjected to both conservative and non-conservative torques.

A. Unperturbed Motion

1. Routh Equations of Motion

Since the Lagrangian (32) does not depend on the spin angle φ, the unperturbed motion has an integral:

$$p_\varphi = const \tag{33}$$

where the generalized impulsep_φ is equal to the projection of the satellite's angular momentum on the spin axis,

$$p_\varphi = \frac{\partial L}{\partial \dot{\varphi}} = A\left(\dot{\varphi} + \dot{\psi}\cos\theta + \Omega\cos\psi\sin\theta\right). \tag{34}$$

Further, the Lagrangian (32) does not depend on the time explicitly, so the Hamiltonian of the unperturbed system is also a constant:

$$\begin{aligned} H &= \sum_{k=1}^{2}\frac{\partial R}{\partial q_k}\dot{q}_k - R = const \\ &= \frac{1}{2}C\left(\dot{\theta}^2 + \dot{\psi}^2\sin^2\theta\right) - \frac{1}{2}C\Omega^2\left(\cos^2\theta\cos^2\psi + \sin^2\psi\right) - \left(p_\varphi\Omega + \mathcal{M}\right)\cos\psi\sin\theta \\ &- \frac{3}{2}\left(C - A\right)\Omega^2\sin^2\theta\sin^2\psi + c_r\sum_{j=1}^{n}\frac{1}{j}b_j\cos j\theta \end{aligned} \tag{35}$$

where a constant term $p_\varphi^2/(2A)$ has been omitted. In Eq. (35), R is the Routhian of the system,

$$R = L - p_\varphi\dot{\varphi}, \tag{36}$$

from which the equations of the unperturbed motion can be found using the standard procedure [45]:

$$\begin{aligned}&\frac{d}{dt}\frac{\partial R}{\partial \dot{q}_k} - \frac{\partial R}{\partial q_k} = 0,\ k = 1,2,\\&\dot{p}_\varphi = 0.\end{aligned} \tag{37}$$

Solving Eqs. (37) for $\ddot{q}_k$ and dividing the results by $A\Omega^2$ gives the dimensionless equations of the unperturbed motion:

$$\begin{aligned}\gamma\theta'' &= \alpha\bar{M}_\theta + \beta\cos\theta\cos\psi - \frac{3}{2}\sin^2\psi\sin 2\theta - \kappa\psi'\sin\theta + \gamma\left[\left(\frac{1}{2} - \cos 2\psi\right)\sin 2\theta + (2\cos\psi\sin\theta + \cos\theta\psi')\,\psi'\sin\theta\right],\\ \gamma\psi'' &= \kappa\theta'\csc\theta + 2\gamma\left[\sin 2\psi - \theta'\left(\cos\psi + \psi'\cot\theta\right)\right] - \beta\sin\psi\csc\theta - \frac{3}{2}\sin 2\psi,\\ \gamma\varphi'' &= \gamma\left[(\psi'\sin\theta - 4\cos\theta\cos\psi)\sin\psi + \theta'\left(\cos\theta\cos\psi + \psi'\left(\cos\theta\cot\theta + \csc\theta\right)\right)\right] + \beta\sin\psi\cot\theta + \frac{3}{2}\cos\theta\sin 2\psi - \kappa\theta'\cot\theta\end{aligned} \tag{38}$$

where $(\quad)'$ denotes derivatives with respect to the true anomaly ν, and

$$\kappa = \frac{p_\varphi}{A\Omega} = \varphi' + \psi'\cos\theta + \sin\theta\cos\psi, \tag{39}$$

$$\beta = \kappa + \mu, \tag{40}$$

$$\mu = \frac{\mathcal{M}}{A\Omega^2} = \frac{M\mu_0\mu_m}{4A\mu_G\pi}, \tag{41}$$

$$\alpha = \frac{A_r L_r \rho R_0^2}{2A}, \tag{42}$$

$$\gamma = \frac{C}{A} \tag{43}$$

are dimensionless quantities. Note that κ and β remain constant in the case of the unperturbed motion by virtue of Eqs. (33), (39), and (41). This allows to rewrite the integral of motion (33) as

$$\kappa = const \tag{44}$$

or

$$\beta = const. \tag{45}$$

It follows from Eqs. (40) and (41) that, despite that the gyroscopic torque from the spin and the magnetic torque are of a completely different nature, in the case of an axisymmetric magnetic satellite, their joint action is mathematically represented by a single dimensionless parameter β [Eq. (40)], which allows mutual compensation of these torques, since they have the same effect on the satellite. This is due to the fact that, in the unperturbed motion, the magnetic and the gyroscopic torques are determined virtually identically, as each of them is a cross product of a vector aligned with the longitudinal axis of the satellite and a vector perpendicular to the orbital plane. The magnetic torque is a cross product of the satellite's magnetic moment and the Earth's magnetic field [Eq. (16)]. In this study, the former is assumed to be aligned with the longitudinal axis of the satellite [Eq. (17)], and the latter, in the unperturbed motion, for which $i = 0$, is perpendicular to the orbital plane. In its turn, the gyroscopic torque is a cross product of the longitudinal component of the satellite's angular momentum $p_\varphi \hat{\boldsymbol{b}}_1$ and the orbital angular velocity vector $\Omega \hat{\boldsymbol{o}}_2$, the latter perpendicular to the orbital plane.

It is worth noting that the integrals of motion (33), (35), (44), (45) contain terms coming from all the three torques considered: aerodynamic, gravitational, and magnetic. As it has been mentioned in the Introduction, this determines the novelty of the present study.

2. Dynamic Potential

The Hamiltonian (35) can be rewritten in the following form:

$$H = T^* + U = const \tag{46}$$

where $T^* = \frac{1}{2}C\left(\dot{\theta}^2 + \dot{\psi}^2\sin^2\theta\right)$ is the part of the kinetic energy that is quadratic in the generalized velocities, and U is the dynamic potential, which depends only on the generalized coordinates and not on the generalized velocities:

$$U = c_r \sum_{j=1}^{n} \frac{1}{j} b_j \cos j\theta - \frac{3}{2}(C - A)\,\Omega^2 \sin^2\theta \sin^2\psi - \frac{1}{2}C\Omega^2\left(\cos^2\theta\cos^2\psi + \sin^2\psi\right) - \left(p_\varphi\Omega + \mathcal{M}\right)\sin\theta\cos\psi. \tag{47}$$

For simplicity, the dynamic potential can be represented in dimensionless form:

$$\begin{aligned}\bar{U} &= \frac{U}{A\Omega^2} \\ &= \alpha \sum_{j=1}^{n} \frac{1}{j} b_j \cos j\theta + \frac{3}{2}(1-\gamma)\sin^2\theta\sin^2\psi - \frac{1}{2}\gamma\left(\cos^2\theta\cos^2\psi + \sin^2\psi\right) - \beta\sin\theta\cos\psi\end{aligned} \tag{48}$$

where each term corresponds to a potential energy of a different nature: the first term represents the potential energy due to the aerodynamic restoring torque, the second is related to the action of the gravitational torque, the third term stands for the potential energy due to the inertial gyroscopic torque from the orbital rotation, and the last term combines the potential energy due to the gyroscopic torque from the spin and the magnetic torque. Eq. (48) describes a large variety of shapes of the potential surface, depending on the coefficients α, β, γ, and b_j. Some of these shapes are considered in the case study [Section IV].

3. Critical Points

The critical points C of the dynamic potential are characterized by $\dot{\theta} = \dot{\psi} = 0$, and are defined by the equations

$$\left.\frac{\partial \bar{U}}{\partial \psi}\right|_{at\ C} = 0, \tag{49}$$

$$\left.\frac{\partial \bar{U}}{\partial \theta}\right|_{at\ C} = 0, \tag{50}$$

or, explicitly,

$$[\beta + (3 - 4\gamma)\sin\theta\cos\psi]\sin\theta\sin\psi = 0, \tag{51}$$

$$\alpha\bar{M}_\theta + \beta\cos\theta\cos\psi - \frac{1}{2}\left[\gamma + (3-4\gamma)\sin^2\psi\right]\sin 2\theta = 0. \tag{52}$$

These general equations describe the following three groups of critical points.

Group C_1. For this group, $\sin\psi \neq 0$. In this case, the equilibrium angular positions $\psi = \psi_1$ and $\theta = \theta_1$ satisfy the following system of equations:

$$\beta + (3 - 4\gamma)\sin\theta\cos\psi = 0, \tag{53}$$

$$\alpha\bar{M}_\theta - \frac{3}{2}(1-\gamma)\sin 2\theta = 0. \tag{54}$$

Note that Eq. (53) directly follows from Eq. (51), since, for the chosen set of Euler angles, $0 < \theta < \pi$. Then solving Eq. (53) with respect to β and substituting the result into Eq. (52) leads to Eq. (54). It follows from Eq. (53) that

$$\psi_1 = \pm\arccos\frac{\beta\csc\theta_1}{4\gamma - 3} \tag{55}$$

where θ_1 is the angle of attack corresponding to the critical points C_1, which can be found from Eq. (54). Clearly, the critical points C_1 exist only if

$$-\beta_{\text{crit}} \leq \beta \leq \beta_{\text{crit}} \tag{56}$$

where

$$\beta_{\text{crit}} = (4\gamma - 3)\sin\theta_1. \tag{57}$$

It is worth noting that, when $\beta = 0$, the system of equations (53) and (54) has an infinite number of solutions, for which ψ_1 is arbitrary and $\theta_1 = 0$ or $\theta_1 = \pi$. This case cannot be modeled using the chosen set of Euler angles, but such motion is highly unlikely to occur in practice, therefore, it is not considered in this study.

Group C_2. For this group, $\psi = \psi_2 = 0$, and $\theta = \theta_2$ can be found from the equation

$$\alpha \bar{M}_\theta + \beta \cos\theta - \frac{1}{2}\gamma \sin 2\theta = 0. \tag{58}$$

Group C_3. For this group, $\psi = \psi_3 = \pm\pi$ and $\theta = \theta_3$ satisfies the equation

$$\alpha \bar{M}_\theta - \beta \cos\theta - \frac{1}{2}\gamma \sin 2\theta = 0. \tag{59}$$

Both Eqs. (58) and (59) follow from Eq. (52) with the substitutions $\psi = \psi_2 = 0$ and $\psi = \psi_3 = \pm\pi$, respectively. Since $\bar{M}_\theta$ [Eq. (10)] and $\sin 2\theta$ are odd functions of θ, the roots of the Eqs. (58) and (59) are related as follows:

$$\theta_3(\beta) = \theta_2(-\beta). \tag{60}$$

Note that the critical points C_2 and C_3 correspond to the case when the satellite's longitudinal axis lies in the local horizontal plane (Fig. 2), since, at these points, the precession angle ψ is equal 0 or $\pm\pi$. This is not the case for the critical points C_1, for which the precession angle can take any value. It should be also mentioned that Eqs. (53), (54), (58), (59), which describe the critical points from all three groups, are consistent with the results of other researchers [15] and generalize these results to the case of an axisymmetric magnetic satellite.

Each critical point can be a maximum, a minimum, or a saddle point of the dynamic potential. The maxima and minima respectively correspond to the unstable and stable equilibrium positions of the satellite's longitudinal axis. The condition for a critical point to be a maximum is

$$\det \mathcal{H} > 0, \operatorname{tr} \mathcal{H} < 0, \tag{61}$$

the condition for a minimum is

$$\det \mathcal{H} > 0, \operatorname{tr} \mathcal{H} > 0, \tag{62}$$

and the condition for a saddle point is

$$\det \mathcal{H} < 0 \tag{63}$$

where

$$\mathcal{H} = \begin{pmatrix} \dfrac{\partial^2 \bar{U}}{\partial \theta^2} & \dfrac{\partial^2 \bar{U}}{\partial \theta \partial \psi} \\ \dfrac{\partial^2 \bar{U}}{\partial \psi \partial \theta} & \dfrac{\partial^2 \bar{U}}{\partial \psi^2} \end{pmatrix} \tag{64}$$

is the Hessian matrix of the dimensionless dynamic potential.

B. Perturbed Motion

The equations of motion for the perturbed system are

$$\frac{d}{dt}\frac{\partial L}{\partial \dot{q}_k} - \frac{\partial L}{\partial q_k} = Q_k, \quad k = 1, 2, 3 \tag{65}$$

where the generalized forces Q_k are

$$Q_k = \frac{\partial}{\partial \dot{q}_k}\left[(\boldsymbol{M}_d + i\boldsymbol{M}_{NC})\cdot\boldsymbol{\omega}\right] \tag{66}$$

where the vectors $\boldsymbol{M}_d$, $\boldsymbol{\omega}$ are defined by Eqs. (12), (14), respectively. The generalized forces can be written as

$$Q_k = A\Omega^2\bar{Q}_k, \tag{67}$$

$$\begin{aligned}
\bar{Q}_1 &= \delta\bar{M}_2^{\omega_2}\left(\cos\theta\cos\varphi\cos\psi - \sin\varphi\sin\psi + \theta'\sin\varphi - \psi'\cos\varphi\sin\theta\right)\sin\varphi \\
&\quad + \delta\bar{M}_3^{\omega_3}\left(\theta'\cos\varphi + \psi'\sin\theta\sin\varphi - \cos\theta\cos\psi\sin\varphi - \cos\varphi\sin\psi\right)\cos\varphi - \varepsilon\left(\cos\nu\sin\theta + 2\cos\theta\sin\nu\sin\psi\right), \\
\bar{Q}_2 &= \delta[\bar{M}_1^{\omega_1}\kappa\cos\theta + \bar{M}_2^{\omega_2}\left(\psi'\cos\varphi\sin\theta - \theta'\sin\varphi + \sin\varphi\sin\psi - \cos\theta\cos\varphi\cos\psi\right)\cos\varphi\sin\theta] \\
&\quad + \delta\bar{M}_3^{\omega_3}\left(\theta'\cos\varphi + \psi'\sin\theta\sin\varphi - \cos\theta\cos\psi\sin\varphi - \cos\varphi\sin\psi\right)\sin\theta\sin\varphi - 2\varepsilon\cos\psi\sin\theta\sin\nu, \\
\bar{Q}_3 &= \delta\bar{M}_1^{\omega_1}\kappa
\end{aligned} \tag{68}$$

where

$$\delta = \frac{A_r L_r^2 \rho R_0}{2A}, \tag{69}$$

$$\varepsilon = \mu i \tag{70}$$

are dimensionless parameters. In Eq. (70), the quantity μ is determined by Eq. (41). Taking into account Eqs. (39)–(42) and (67)–(70), the equations of perturbed motion (65) can be represented in the dimensionless form

$$\begin{aligned}
\gamma\theta'' &= \alpha\sum_{j=1}^{n} b_j\sin j\theta + \beta\cos\theta\cos\psi - \frac{3}{2}\sin^2\psi\sin 2\theta - \kappa\psi'\sin\theta + \gamma\left[\left(\frac{1}{2} - \cos 2\psi\right)\sin 2\theta + \left(2\cos\psi\sin\theta + \psi'\cos\theta\right)\psi'\sin\theta\right] \\
&\quad + \delta f_1\left(\psi, \psi', \theta, \theta', \varphi\right) + \varepsilon g_1\left(\psi, \theta, \varphi, \nu\right), \\
\gamma\psi'' &= \kappa\theta'\csc\theta + 2\gamma\left[\sin 2\psi - \theta'\left(\cos\psi + \psi'\cot\theta\right)\right] - \beta\sin\psi\csc\theta - \frac{3}{2}\sin 2\psi \\
&\quad + \delta f_2\left(\psi, \psi', \theta, \theta', \varphi\right) + \varepsilon g_2\left(\psi, \theta, \varphi, \nu\right), \\
\gamma\varphi'' &= \gamma[\left(\psi'\sin\theta - 4\cos\theta\cos\psi\right)\sin\psi + \theta'\left(\cos\theta\cos\psi + \psi'\left(\cos\theta\cot\theta + \csc\theta\right)\right)] + \beta\sin\psi\cot\theta + \frac{3}{2}\cos\theta\sin 2\psi - \kappa\theta'\cot\theta \\
&\quad + \delta f_3\left(\psi, \psi', \theta, \theta', \varphi, \varphi'\right)
\end{aligned} \tag{71}$$

where δf_k and εg_k are respectively perturbations from the aerodynamic damping and the non-conservative component of the magnetic torque. Note that, in contrast to the unperturbed motion, the dimensionless quantities κ and β, which are still defined by Eqs. (39) and (40), respectively, are no longer constant in the perturbed motion.

IV. Case Study

In this section, we will present an example axisymmetric aerodynamically stabilized satellite, analyze the critical points of its unperturbed dynamic potential, numerically simulate the perturbed motion, and finally visualize the simulation results using Poincaré sections. Due to the complexity of the connections between its different parts, this section starts from a visual guide shown in Fig. 3. This schematic guide is intended to help the reader follow the logical sequence of all the steps taken.

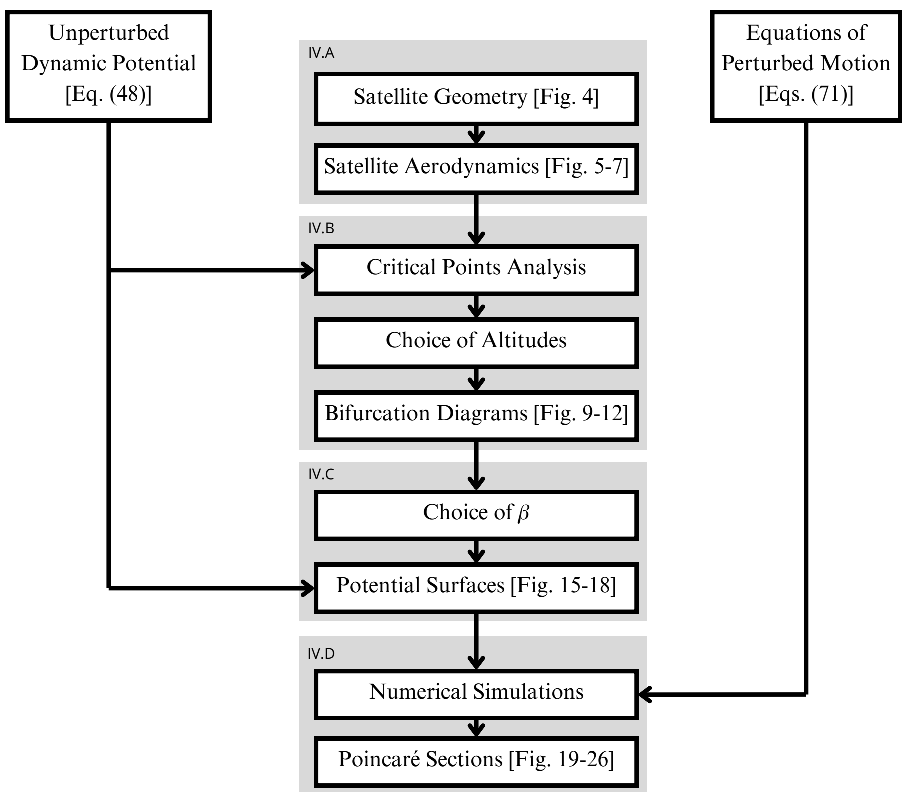

Fig. 3 Visual guide to Section IV.

A. Example Satellite

Consider an axisymmetric magnetic satellite in LEO/VLEO, whose shape is similar to the one of the vehicle discussed in Ref. [46]. The example satellite has three parts: a body, a conic membrane, and an inflatable torus (Fig. 4). The body is a cylinder with a length 0.4 m and a base diameter 0.2 m, equipped with a hemispherical nose of a radius 0.1 m. The aeroshell has a diameter of 1.05 m and a flare angle of 65°. The inflatable torus is a tube of a diameter of 0.15 m. The overall diameter of the vehicle is $L_r = 2r = 1.3$ m with a corresponding area $A_r = \pi r^2 = 1.33$ m^2. These two values are used for the calculation of the aerodynamic coefficients as reference length and reference area, respectively. The center of mass of the satellite is considered to coincide with the body's geometric center. The longitudinal and transverse moments of inertia are $A = 0.01$ kg $\cdot$ m^2 and $C = 0.1$ kg $\cdot$ m^2, respectively.

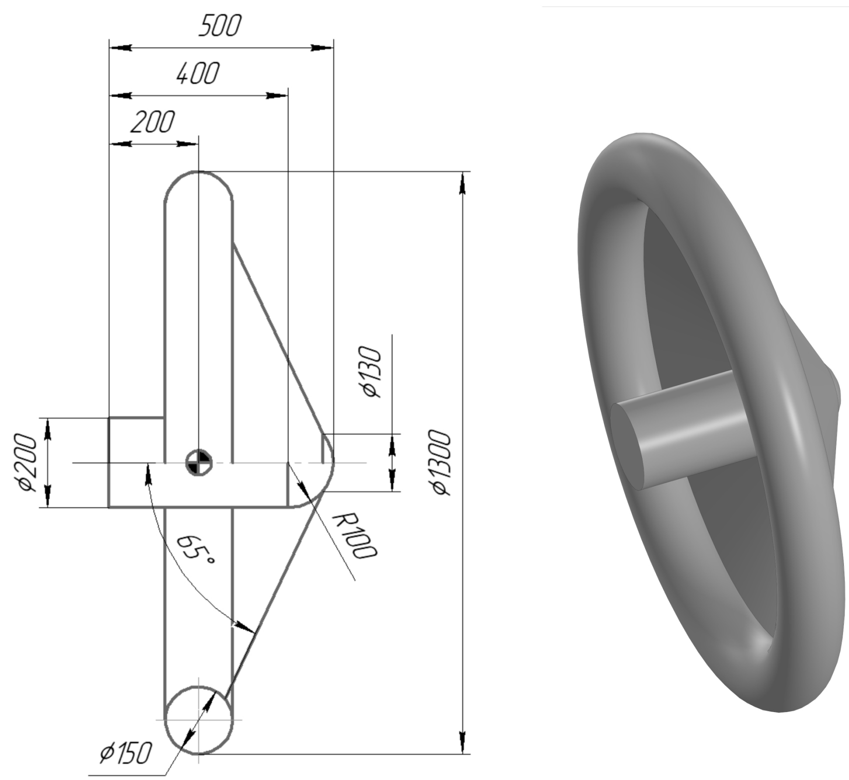

Fig. 4 Example satellite.

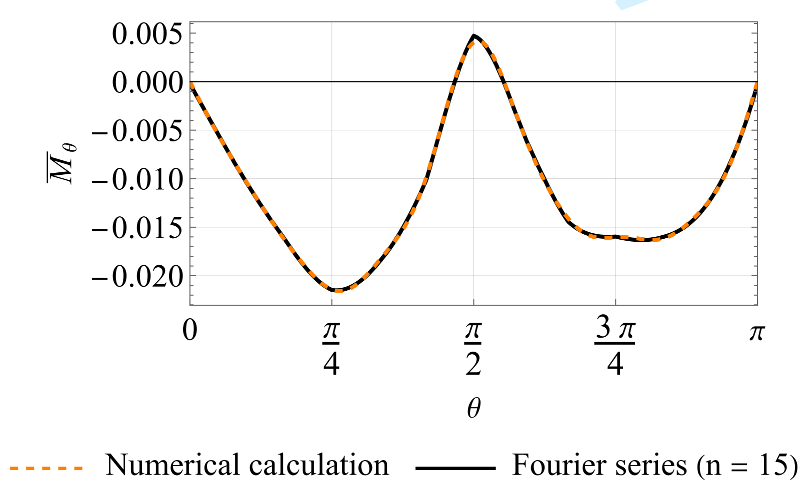

Fig. 5 Coefficient of restoring aerodynamic torque.

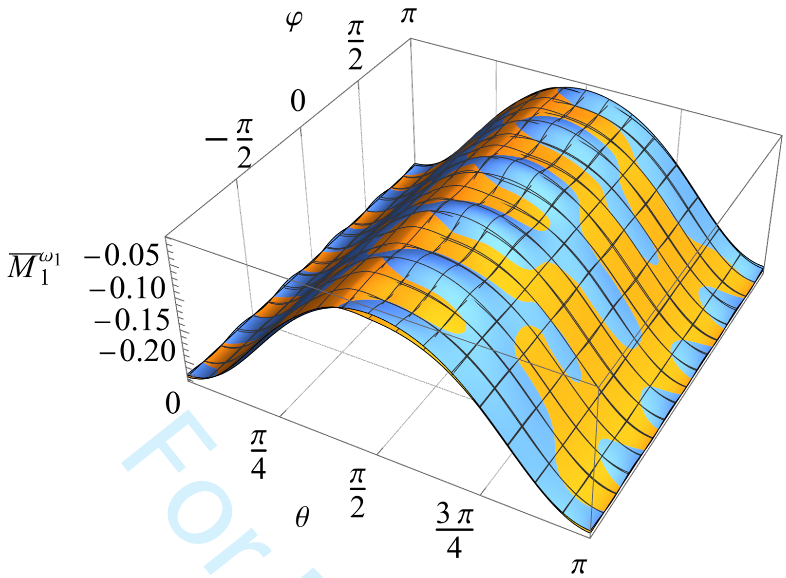

Fig. 6 The damping aerodynamic torque coefficient $\bar{M}_1^{\omega_1}$.

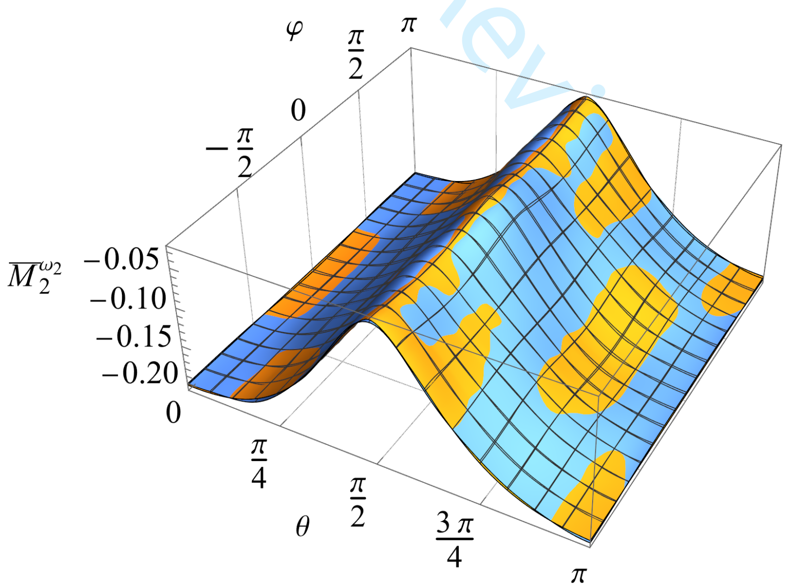

Fig. 7 The damping aerodynamic torque coefficient $\bar{M}_2^{\omega_2}$.

The aerodynamic coefficients of the satellite were calculated by dividing its surface into triangular elements, calculating the normal and tangential coefficients assuming a free-molecular flow [32, 47, 48], and integrating these coefficients over the entire surface. Fig. 5 represents the results of the numerical calculation of the coefficient of restoring aerodynamic torque $\bar{M}_\theta$, as well as an approximation of these results by a Fourier series [Eq. (10)]. The same information regarding the coefficients of the damping torque is shown in Figs. 6 and 7. Note that this time the approximation is made by means of a 2D Fourier series [Eqs. (15)]. By virtue of the last of Eqs. (15), the plot for $\bar{M}_3^{\omega_3}$ is redundant and thus is not shown.

B. Critical Points Analysis. 3D Bifurcation Diagrams

Equations (49) and (50) describing the critical points of the dynamic potential have a rich and complicated solution structure to be revealed in the present section. If the satellite is specified, then the number, location, and stability of the critical points depend on only two constant parameters: the orbital altitude h and dimensionless parameter β [Eq. (40)]. The analysis of the critical points of the example satellite implies (1) calculation of the critical points belonging to all three groups, introduced in Subsection III.A.3, by solving Eqs. (53),(54), (58), (59) for different values of h and β; (2) determination of the character of each point using the conditions (61)–(63). This analysis will allow to choose some combinations of h and β that give typical shapes of the dynamic potential useful for practical purposes. On the other hand, we will also look for complicated shapes of the potential having multiple equilibrium positions and, most importantly, saddle points. The attitude motion near these points, in the presence of perturbations, may be chaotic and is therefore of particular interest.

It is convenient to start the analysis of the critical points from the determination of the angles of attack θ_1 corresponding to Group C_1. For a specific satellite, these angles depend only on the altitude and are determined by Eq. (54). Fig. 8 depicts the angles θ_1 for the example satellite, which form two distinct sets $\theta_{1,\mathrm{I}}$ and $\theta_{1,\mathrm{II}}$,

$$\begin{aligned} &\pi/2 \le \theta_{1,\mathrm{I}} < \pi, \\ &0 < \theta_{1,\mathrm{II}} < \pi/2. \end{aligned} \tag{72}$$

It can be seen from Fig. 8 that, for the example satellite, the angle of attack $\theta_{1,\mathrm{I}}$ varies with altitude quite slowly. A more complicated dependence on altitude is demonstrated by the set $\theta_{1,\mathrm{II}}$, especially at $h_3 = 613$ km, where there are five critical points, two of them being saddles, so let us choose this altitude for further analysis. Fig. 8 also illustrates an interesting fact that there are no critical points in the set $\theta_{1,\mathrm{II}}$ above a certain altitude. This can be explained as follows. The angles of attack corresponding to the critical points C_1 shown in Fig. 8 are determined by Eq. (54), the left-hand side of which is actually a sum of all pitch torques. The first term is the aerodynamic torque, the second one represents the gravitational torque. At VLEO altitudes, where the air is dense and consequently where the parameter α [Eq. (42)] is high, the first term dominates, so the critical points in this case are basically the two roots of the pitch torque coefficient M_θ (see Fig. 5), which satisfy the condition $0 < \theta < \pi$. At high altitudes, α is very close to zero, thus, the second term dominates on the left-hand side of Eq. (54), meaning that there is only one root, the one that is close to $\pi/2$. Thus, there should be an altitude, above which the satellite has only one critical point of the type C_1. Clearly, this altitude depends on the satellite parameters. For the example satellite, it is about 615 km. Another interesting altitude for an aerodynamically stabilized satellite is $h_1 = 200$ km, which corresponds to the VLEO region. To make the further analysis more general, we will also consider the altitudes $h_2 = 400$ km and $h_4 = 800$ km, which, together with h_1 and h_3, form a set of four almost equally spaced altitudes. The labels *a*–*j* in Fig. 8 denote the all critical points C_1 at the altitudes of interest. These labels will be used in the following figures in order to facilitate their perception by the reader and highlight interconnections.

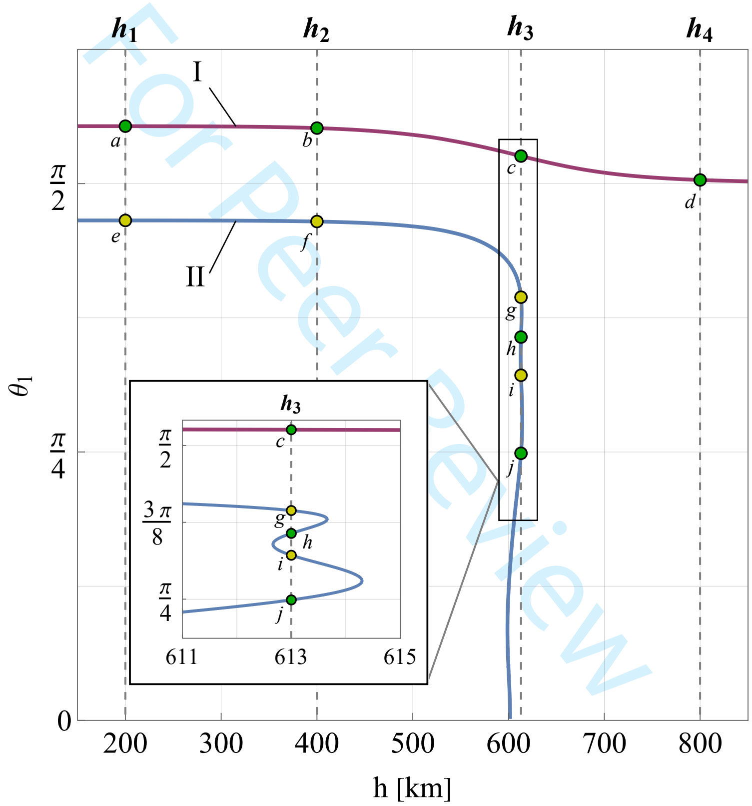

Fig. 8 Angles of attack corresponding to the critical points C_1 [Eq. (54)]. Yellow: saddle points; green: stable equilibrium. Labels *a*–*j* refer to the curves marked in Figs. 9–13.

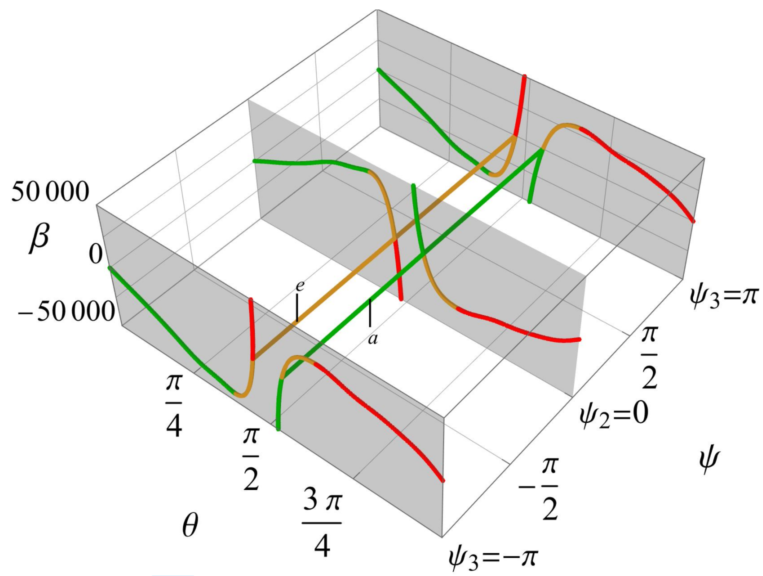

Fig. 9 Bifurcation diagram for critical points at h_1 = 200 km. Red: unstable equilibrium; yellow: saddle points; green: stable equilibrium. Labels *a*, *e* correspond to the points C_1 marked in Figs. 8 and 13.

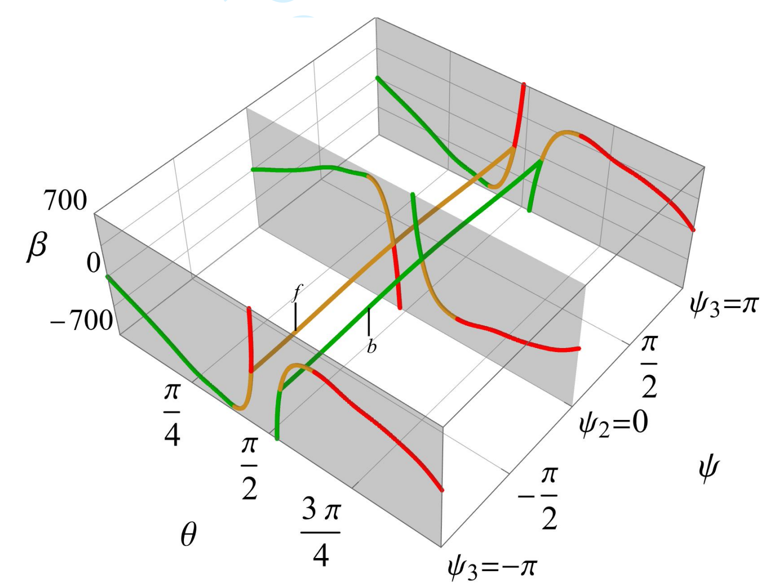

Fig. 10 Bifurcation diagram for critical points at h_2 = 400 km. Red: unstable equilibrium; yellow: saddle points; green: stable equilibrium. Labels *b*, *f* correspond to the points C_1 marked in Figs. 8 and 13.

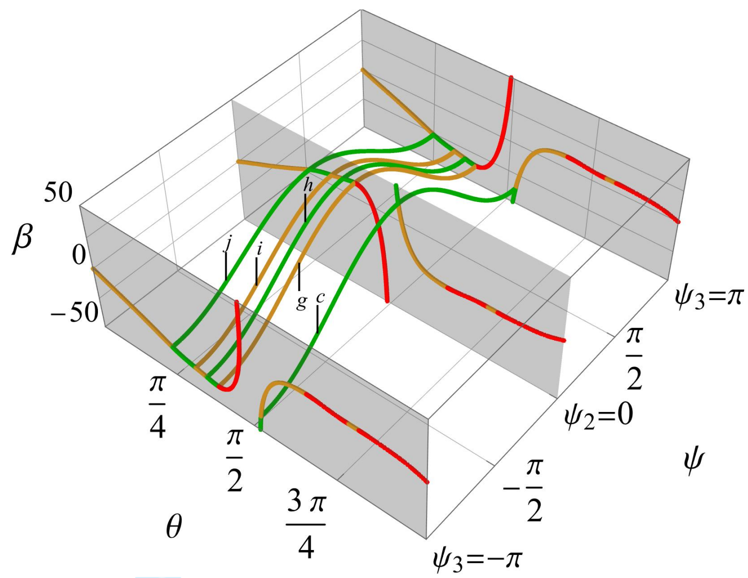

Fig. 11 Bifurcation diagram for critical points at $h_3 = 613$ km. Red: unstable equilibrium; yellow: saddle points; green: stable equilibrium. Labels *c*, *g*–*j* correspond to the points C_1 marked in Figs. 8 and 13.

Once the altitudes of interest $h_1 ... h_4$ are chosen, one can draw a three-dimensional bifurcation diagram for each of these altitudes in a 3D space (θ, ψ, β) with β as parameter (Figures 9–12). The bifurcation diagrams depict the critical points from all three groups and are formed by the solutions of Eqs. (53),(54), (58), (59). The character of each point was determined using the conditions (61)–(63). In Figures 9–12, as in all figures in this section, the following color coding is used: red for unstable points, yellow for saddles, and green for stable points. In order to highlight different groups of critical points in the overall bifurcation diagrams, Figures 9–12 have some additional elements. The labels *a*–*j* mark the curves that are formed by the critical points of Group C_1 only, while the gray planes $\psi = 0$ and $\psi = \pm\pi$ highlight the critical points from Groups C_2 and C_3, respectively.

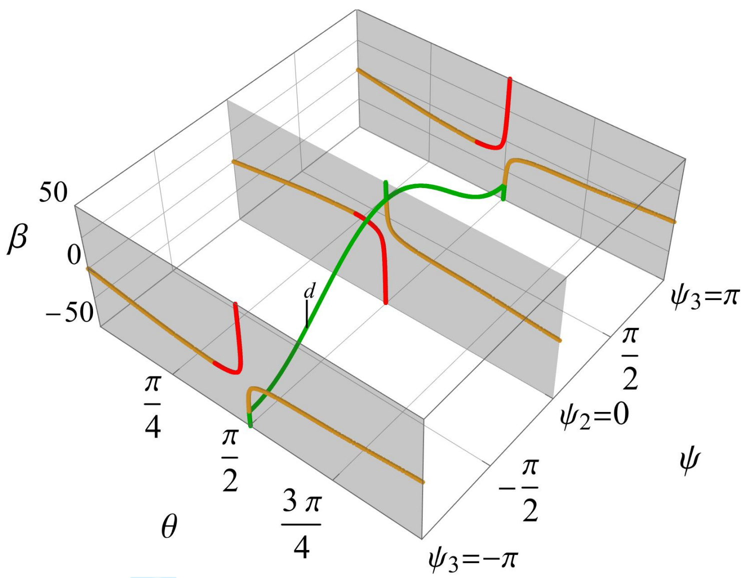

Fig. 12 Bifurcation diagram for critical points at h_4 = 800 km. Red: unstable equilibrium; yellow: saddle points; green: stable equilibrium. Label *d* corresponds to the points C_1 in Figs. 8 and 13.

The analysis of the three-dimensional bifurcation diagrams allows making a general remark that at each of the altitudes of interest the example satellite has at least one stable equilibrium position, regardless of the value of β. A typical evolution of a stable point C_i with growing β is the following: (C_3 for $\beta < -\beta_{crit}$) $\rightarrow$ (C_1 for $-\beta_{crit} \leq \beta \leq \beta_{crit}$) $\rightarrow$ (C_2 for $\beta > \beta_{crit}$) where β_{crit} is determined by Eq. (57). The bifurcation diagram for 800 km is the simplest, since it only has one stable C_1 curve. The diagrams for altitudes of 400 km and 200 km have similar, but more complicated structure, now with one stable and one unstable C_1 curves. The richest bifurcation diagram corresponds to the altitude of 613 km, since it includes five C_1 curves, of which three are stable and two are unstable. Note that, at all altitudes, each intersection of the C_2 curve with a C_1 curve changes the stability character of the former; this is also true for the C_3–C_1 intersections.

Figures 13 and 14 are meant to provide additional perspectives on the dependencies of ψ_1 and θ_2 on h and β, being projections of the three-dimensional bifurcation curves on different planes in a 3D space (θ, ψ, β). The projection of C_1 curves on the plane (β, ψ) shown in Fig. 13 illustrates the above-mentioned fact that the C_1 points exist in a rather narrow diapason of β, as follows from Eq. (56). Figure 14 represents a projection of the C_2 curves on the plane (β, θ) emphasizing that the angles θ_2 form two distinct sets $\theta_{2,\mathrm{A}}$ and $\theta_{2,\mathrm{B}}$,

$$\begin{aligned} \pi/2 \leq \theta_{2,\mathrm{A}} < \pi, \\ 0 < \theta_{2,\mathrm{B}} \leq \pi/2. \end{aligned} \tag{73}$$

The graphs $\theta_3(\beta)$ are not shown, since by virtue of Eq. (60) they are simply $\theta_2(\beta)$ curves (Fig. 14) mirrored with respect to the ordinate axis.

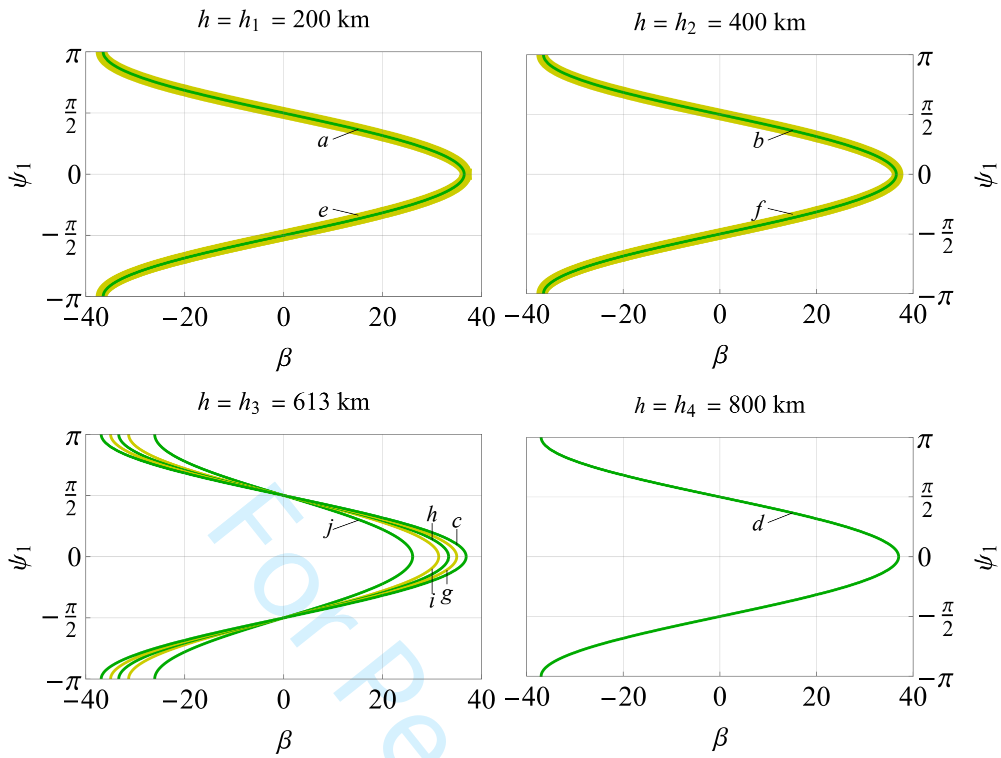

Fig. 13 Precession angles corresponding to the critical points C_1 [Eq. (55)]. Yellow: saddle points; green: stable equilibrium. Labels *a–j* correspond to the points marked in Fig. 8.

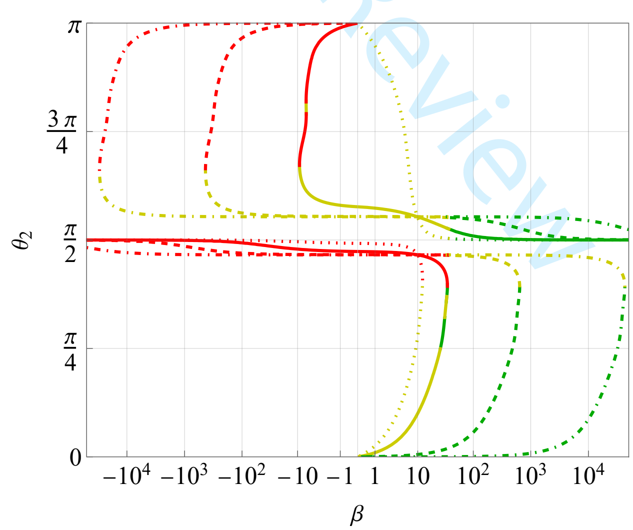

Fig. 14 Angles of attack corresponding to the critical points C_2 [Eq. (58)]. Red: unstable equilibrium; yellow: saddle points; green: stable equilibrium. Dotted dashed: 200 km, dashed: 400 km, solid: 613 km, dotted: 800 km.

C. Unperturbed Dynamic Potential Surfaces

The dimensionless dynamic potential is of significant importance to the intuitive perception of the possible attitude motions of the satellite, since, for small perturbations, the projections of the phase trajectories of the satellite on the (θ, ψ) plane will closely follow the equipotential lines.

Figures 13 and 14 allow choosing the particular values of the dimensionless quantity β for the visualizations of the dimensionless dynamic potential to be presented in the present subsection. Namely, we choose for $h = h_1 = 200$ km $\beta = 5000; 25000; 50000$; for $h = h_2 = 400$ km $\beta = 10; 30; 100$; for the other altitudes, $\beta = 5; 30; 40$. The choice of higher values of β for lower altitudes is substantiated by the fact that, the lower the orbit, the higher the possible initial values of the spin rate φ' which contributes to the value of β (see Eqs. (39), (40)). In the authors' opinion, the values chosen allow, on the one hand, to demonstrate the peculiarities of the evolution of the potential with changing β, and, on the other hand, to show some typical and some unusual shapes of the potential.

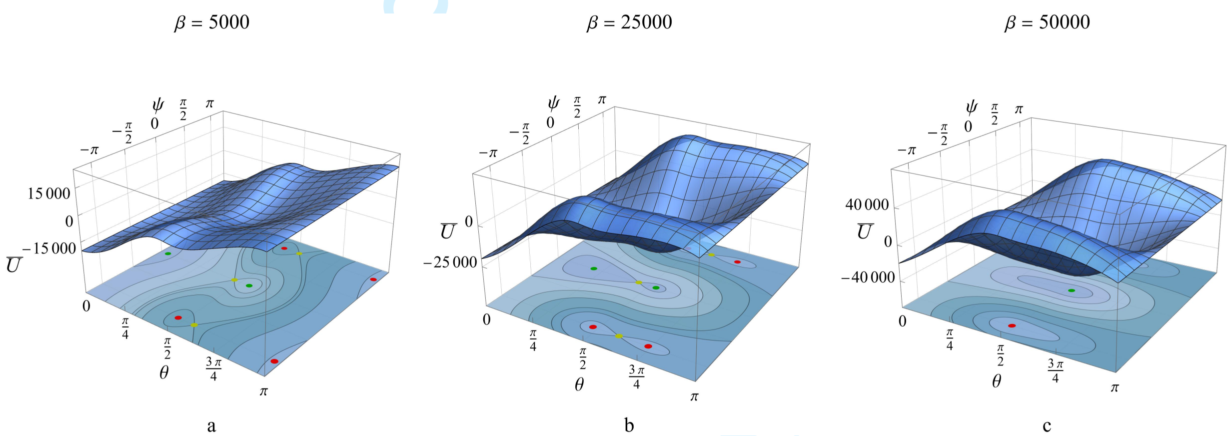

Fig. 15 Dimensionless dynamic potential ($h = h_1 = 200$ km). Red dots: unstable equilibrium; yellow dots: saddle points; green dots: stable equilibrium.

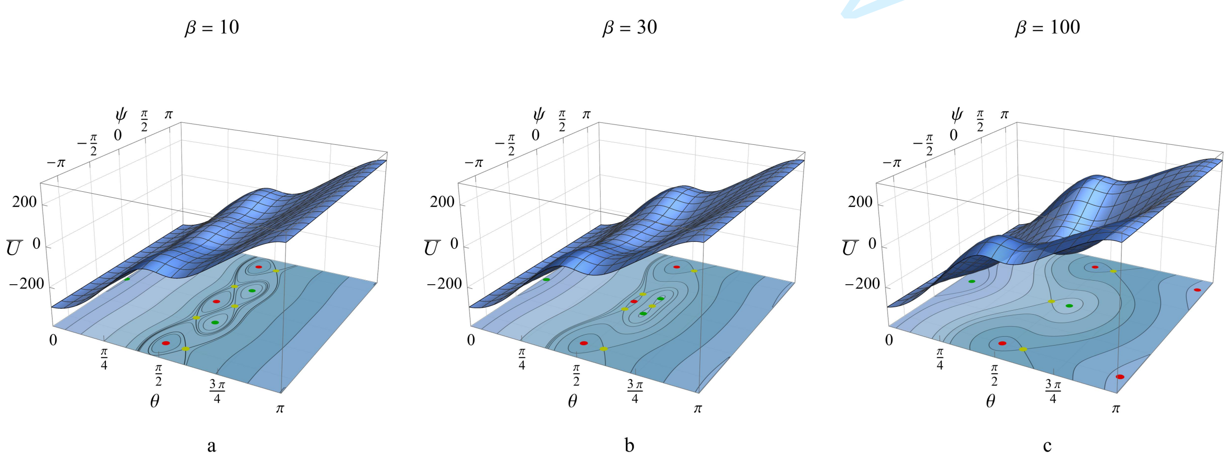

Fig. 16 Dimensionless dynamic potential ($h = h_2 = 400$ km). Red dots: unstable equilibrium; yellow dots: saddle points; green dots: stable equilibrium.

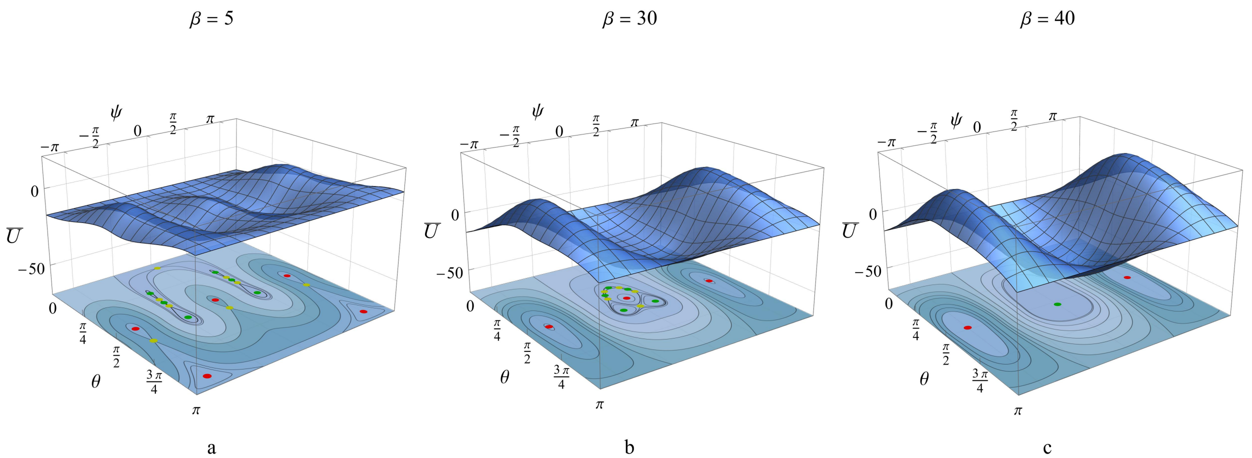

Fig. 17 Dimensionless dynamic potential ($h = h_3 = 613$ km). Red dots: unstable equilibrium; yellow dots: saddle points; green dots: stable equilibrium.

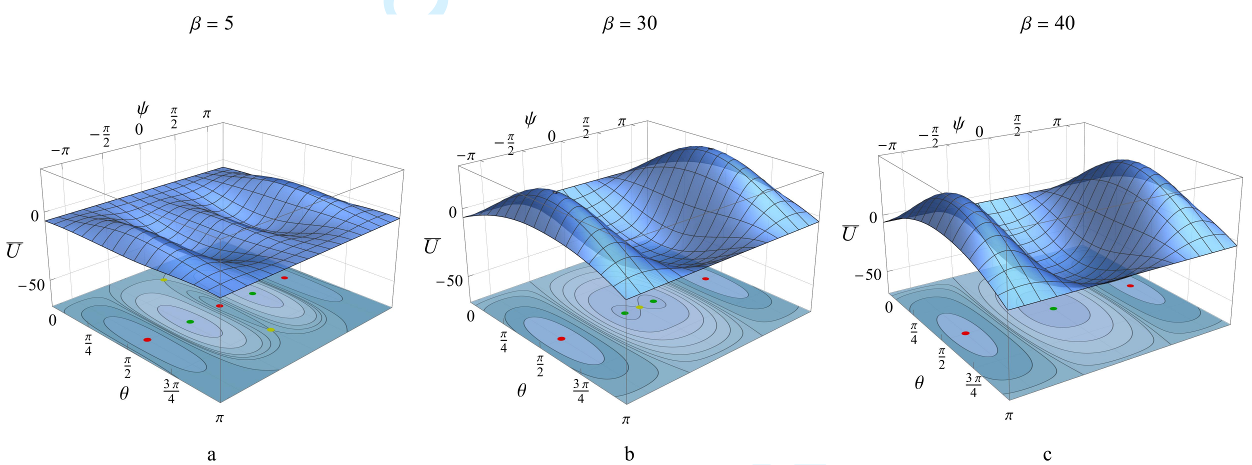

Fig. 18 Dimensionless dynamic potential ($h = h_4 = 800$ km). Red dots: unstable equilibrium; yellow dots: saddle points; green dots: stable equilibrium.

Figures 15–18 illustrate an evolution of the dynamic potential surfaces for the values of the parameter β chosen above. The contour plots of the dynamic potential shown below the surfaces can be interpreted as projections of the phase diagrams of the unperturbed motion on the plane (θ, ψ). In each contour plot, the corresponding critical points of the potential are shown. Hereinafter, the unstable equilibrium positions are marked in red, the saddle points are yellow, and the green dots represent the stable equilibrium positions. Note that the equipotential lines passing through the saddle points are the separatrices of the unperturbed phase space. From the analysis of the changing shape of the surfaces and the equipotential curves, it can be seen that, as previously discussed, the number of critical points and their stability character change significantly with β. Note that in some cases, for example, the ones illustrated by Fig. 16,a,b, Fig. 17,a,b, and Fig. 18,b, inside bigger potential wells there are smaller ones. Clearly, motion in the smaller wells is only possible in the case of relatively weak perturbations.

D. Simulations of Perturbed Motion. Poincaré sections

This section aims to demonstrate that the perturbed motion can be chaotic, in the sense that slight changes in initial conditions can lead to qualitative changes in the attitude motion, such as the passing of the phase trajectory from one potential well to another and back, or sudden precession of the longitudinal axis. To clearly show these phenomena, numerical simulations will be performed for the cases when the unperturbed dynamic potential has complicated shapes, with saddle points lying between different potential wells. Accordingly, based on Figures 15–18, the following simulation parameters have been chosen:

$h = h_4 = 800$ km: $\beta_0 = 30$ (Fig. 18, b);

$h = h_3 = 613$ km: $\beta_0 = 5$ (Fig. 17, a);

$h = h_2 = 400$ km: $\beta_0 = 100$ (Fig. 16, c);

$h = h_1 = 200$ km: $\beta_0 = 25000$ (Fig. 15, b).

Note that the dimensionless quantity β is now written as β_0, in order to emphasize that it is the initial value of the quantity, which does not remain constant in the perturbed motion. The numerical simulations will be performed via the numerical integration of Eqs. (71) using an explicit Runge–Kutta method for different levels of the perturbations due to the orbital inclination, which are characterized by the dimensionless parameter ε [Eq. (70)].

The results of the simulations, which will be illustrated and discussed in detail further, lead to a general conclusion that, with increasing ε, the satellite tends to pass sequentially through the following three regimes of attitude motion:

Regime 1. Satellite remains in the initial potential well.

Regime 2. Satellite passes from one potential well to another without full rotation around the precession axis. The higher the parameter ε, the more distant wells are reached.

Regime 3. Satellite passes from one potential well to another with full rotation(s) around the precession axis.

The last two regimes can be considered chaotic, since whether the satellite passes from one well to another strongly depends on the initial conditions.

1. Altitude 800 km

Figures 19 and 20 depict the projections of Poincaré sections onto the plane (θ, ψ), so each black point in these 2D plots represents a simulated orientation of the satellite's longitudinal axis. For a smaller value of ε (Fig. 19), the satellite is in a regular Regime 1. A higher value of ε transfers the satellite into a chaotic Regime 2, as layers connecting the upper and lower potential wells appear (Fig. 20), meaning that the satellite's longitudinal axis moves in such a way that the phase trajectory passes through both potential wells.

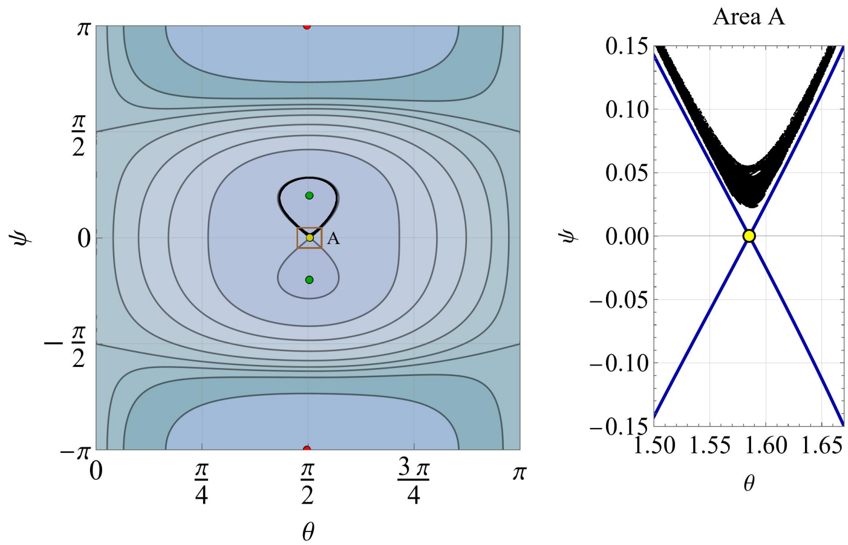

Fig. 19 Poincaré sections ($h = h_4 =$ **800 km,** $\beta = 30$**,** $\varepsilon = 0.01$**).**

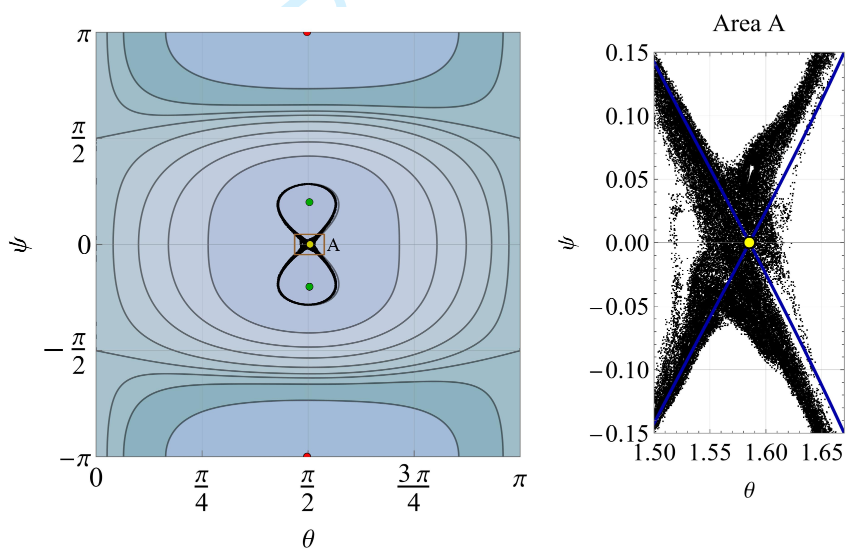

Fig. 20 Poincaré sections ($h = h_4 =$ **800 km,** $\beta = 30$**,** $\varepsilon = 0.25$**).**

2. Altitude 613 km

In this case, illustrated by Fig. 21, all simulations start in a small potential well around the stable point $(1.15; 1.42)$. As in the previous case, weak perturbations cannot cause the satellite to leave the well (Regime 1, Fig. 21, a). Stronger perturbations cause the satellite to move chaotically between the initial well and the two neighboring wells (Regime 2, Fig. 21, b). As the perturbations increase further, the satellite leaves the area around the above-mentioned wells and passes into Regime 3, as the transition between the wells is accompanied by full rotations around the precession axis (Fig. 21, c). In order to illustrate this phenomenon from a slightly different perspective, the Poincaré section points have been projected on an imaginary sphere whose center coincides with the center of mass of the satellite (Fig. 22). Here, again, each black point represents a simulated orientation of the satellite's longitudinal axis. In the authors' opinion, these 3D Poincaré sections, accompanied by the satellite's velocity vector, as well as by the orbital and local horizontal planes, provide a better understanding of the complicated motions discussed.

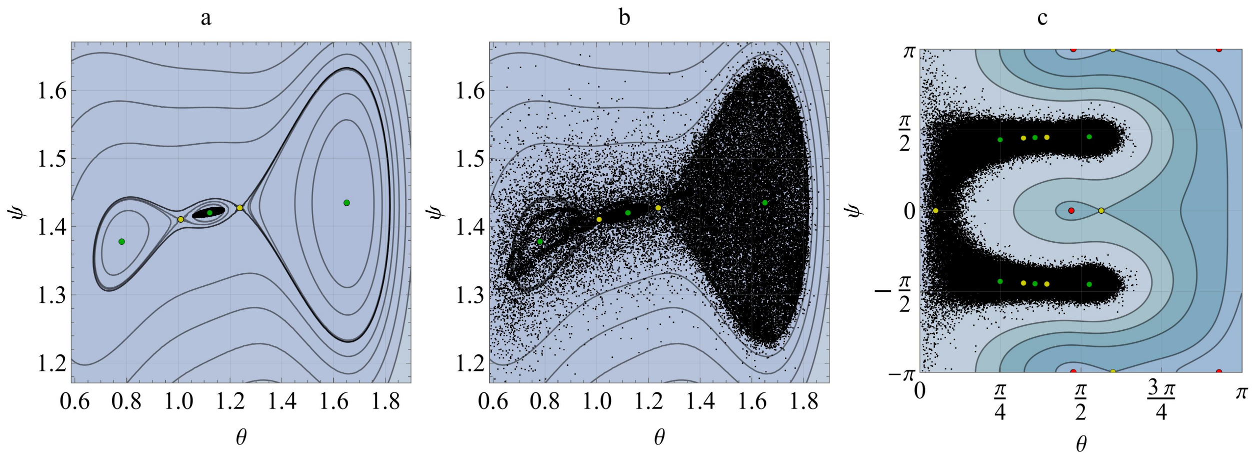

Fig. 21 Poincaré sections ($h = h_3 =$ 613 km, $\beta = 5$): a: $\varepsilon = 0.01$; b: $\varepsilon = 0.1$; c: $\varepsilon = 0.15$.

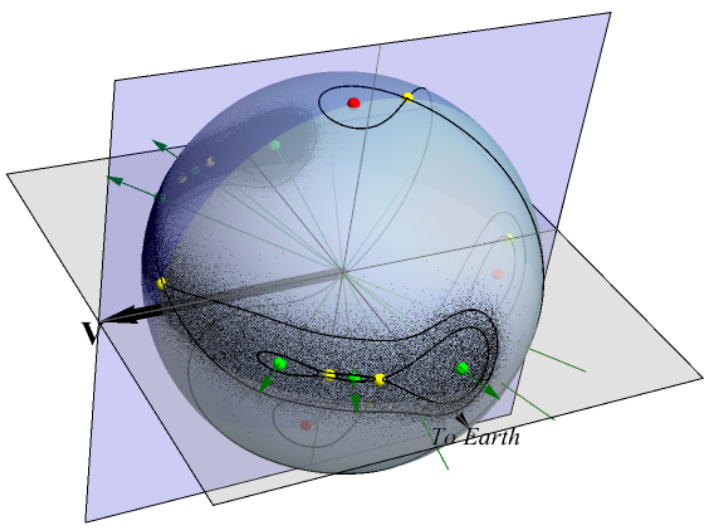

Fig. 22 3D Poincaré sections ($h = h_3 =$ 613 km, $\beta = 5$, $\varepsilon = 0.15$). Green arrows: orientations of the satellite's longitudinal axis corresponding to the stable critical points. The orbital and local horizontal planes are shown in gray and black, respectively.

3. Altitude 400 km

Fig. 23 represents the Poincaré sections made by simulations of the phase trajectories starting in one of the wells of the potential surface, corresponding to the altitude of 400 km. Again, it can be seen that in the case weak perturbations the satellite stays in the initial potential well (Fig. 23, a). Stronger perturbations transfer the satellite into a chaotic

Regime 3, since it can perform full rotations about the precession axis, as shown in Figures 23, b and 24.

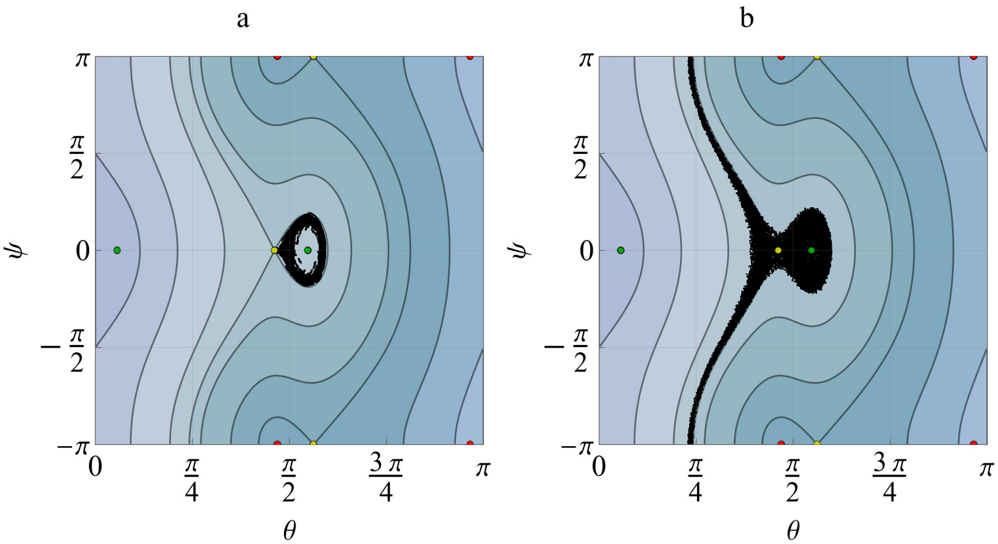

Fig. 23 Poincaré sections ($h = h_2 =$ 400 km, $\beta = 100$): a: $\varepsilon = 1.0$; b: $\varepsilon = 1.01$.

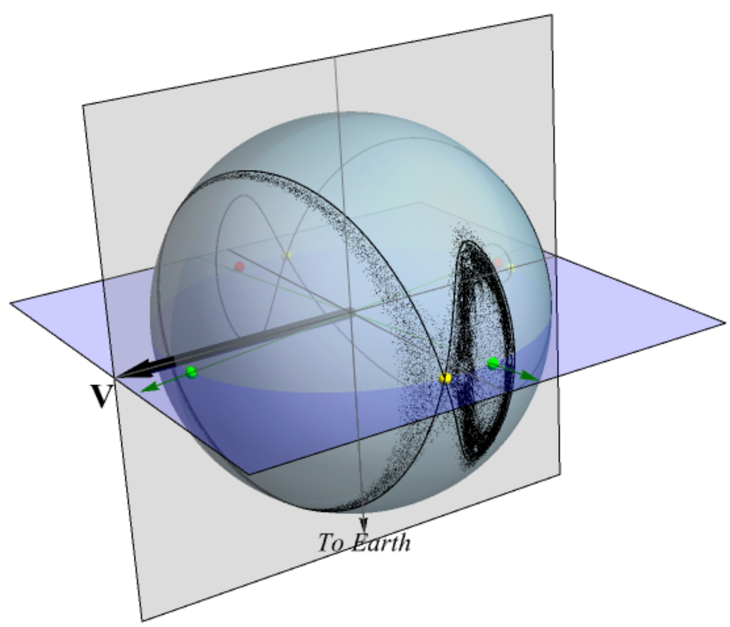

Fig. 24 3D Poincaré sections ($h = h_2 =$ 400 km, $\beta = 100$, $\varepsilon = 1.01$). Green arrows: orientations of the satellite's longitudinal axis corresponding to the stable critical points. The orbital and local horizontal planes are shown in gray and black, respectively.

4. Altitude 200 km (VLEO)

Fig. 25, a depicts Poincaré sections corresponding to an altitude of 200 km for $\varepsilon = 25$. It can be seen that, in VLEO, this level of perturbations is not enough to make the satellite leave the initial potential well. To make the satellite pass to Regime 3 characterized by full rotations of the longitudinal axis about the velocity vector (Fig. 25, b; Fig. 26) one needs to increase the perturbations to $\varepsilon = 50$. Note that such a high value of ε is completely realistic since, e.g., by virtue of Eqs. (41) and (70), for the example satellite in a VLEO orbit with an inclination of 10°, it corresponds to a magnetic dipole strength $M = 0.15$ A·m^2, which is within the capabilities of commercially available nanosatellite magnetorquers.

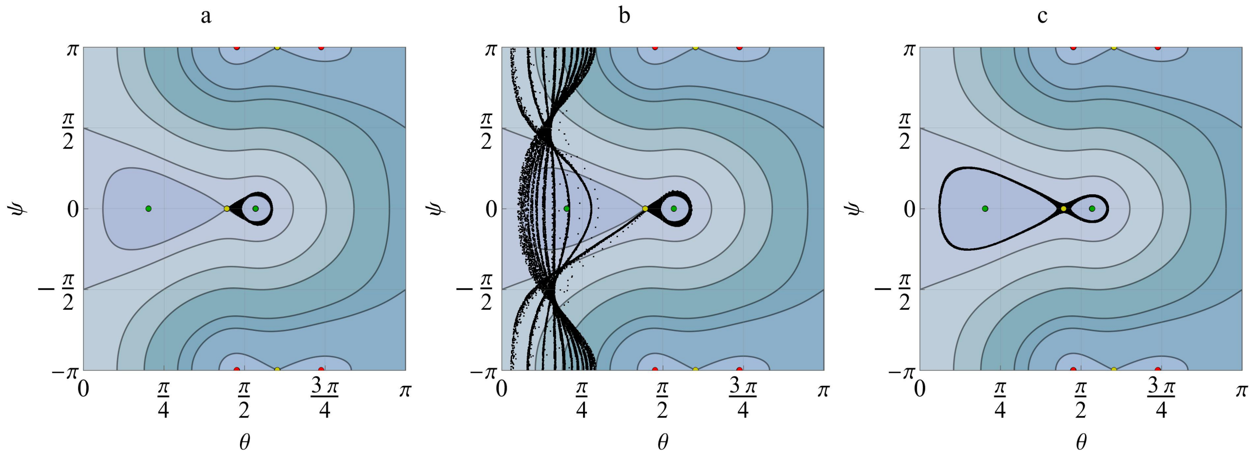

Fig. 25 Poincaré sections ($h = h_1$ **= 200 km,** β = 25000**): a:** $\delta \neq 0$**,** $\varepsilon = 25$**; b:** $\delta \neq 0$**,** $\varepsilon = 50$**; c:** $\delta = 0$ **(aerodynamic damping neglected),** $\varepsilon = 50$**.**

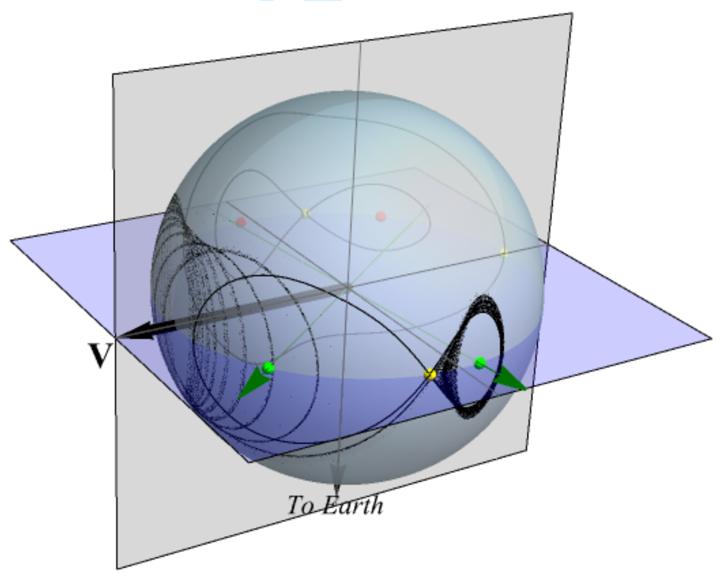

Fig. 26 3D Poincaré sections ($h = h_1$ **= 200 km,** $\beta = 25000$, $\delta \neq 0$, $\varepsilon = 50$**). Green arrows: orientations of the satellite's longitudinal axis corresponding to the stable critical points. The orbital and local horizontal planes are shown in gray and black, respectively.**

Note that at the left part of Fig. 25, b, where the angle of attack is less than about $\pi/4$, the Poincaré section points, unlike in all previously discussed cases, do not follow the isolines of the unperturbed dynamic potential. This is due to the fact that, at VLEO altitudes, for such relatively small angles of attack, the aerodynamic damping torque is noticeably large. Thus, in this particular case, the proposed separation of the attitude motion does not work equally well in the whole (θ, ψ) space. Fig. 25, c, shows the Poincaré sections for the same set of initial conditions as the one used to plot Fig. 25, b but with zero aerodynamic damping torque ($\delta = 0$). Note that, in this idealized case, the Poincaré section points follow the isolines of the unperturbed dynamic potential quite accurately, proving that the peculiar behavior visible in the left part of Fig. 25, b is indeed due to the presence of damping. This shows that, in VLEO simulations, the aerodynamic damping torque cannot be neglected.

Thus, the numerical simulations performed in this section demonstrated that the proposed separation of the attitude motion into unperturbed and perturbed motions is applicable to study the behavior of the aerodynamically stabilized spinning magnetic satellites, except for the case of small angles of attack and strong perturbations in VLEO. Furthermore, we have shown that, in the presence of perturbations due to small orbital inclination, chaotic attitude motion is possible.

V. Conclusion

This study considers the near-equatorial spatial attitude motion of an axisymmetric aerodynamically stabilized magnetic satellite with a more in-depth bifurcation analysis of the critical points of its dynamic potential as well as chaotic regimes of attitude motion.

The new equations of spatial attitude motion for a passive axisymmetric near-equatorial LEO/VLEO satellite derived in the study allow taking into account the combined action of three environmental torques, namely, gravitational, aerodynamic, and magnetic. The proposed separation of the attitude motion into two parts - the unperturbed motion under potential torques and small perturbations due to the non-potential torques - provides a more intuitive understanding of the motion under consideration, as the unperturbed motion is shown to have a dynamic potential. This potential is a function of the two angles that determine the direction of the satellite's longitudinal axis: θ and ψ. Thus, if the perturbations are small or absent, the projection of the phase trajectory onto the (θ, ψ) plane and thus the satellite's longitudinal axis will move according to the dynamic potential's shape, which varies in a complicated way with the above parameters. This justifies the calculation of the position and stability analysis of the critical points of the potential, which was also performed in the present study. Since the dynamic potential and consequently the coordinates θ, ψ of the critical points also depend on the system parameter β and on the orbital altitude, several 3D bifurcation diagrams were made, which allow to study a complex evolution of the critical points of the example satellite in terms of existence and stability. The analysis of the Poincaré sections resulting from the numerical simulations leads to the conclusion that the level of perturbations significantly affects the character of the motion. As the perturbations increase, the system begins to exhibit chaotic behavior.

The results of this study can be used for planning near-equatorial missions involving small passive aerodynamically stabilized magnetic spacecraft, such as satellites with failed control systems, re-entry capsules, or space debris objects, since the proposed framework provides a fundamental classical mechanics-based understanding of their behavior and allows to predict their attitude motion over a wide range of altitudes, which is an indispensable part of any mission design.

Author Contributions

Conceptualization: V.S.A. and D.A.S.; methodology: V.S.A. and D.A.S.; software: D.A.S.; investigation: D.A.S.; writing—original draft: D.A.S.; writing—review and editing: V.S.A. and D.A.S.

References

[1] Haldar, S., "Chapter 6 - Photogeology, Remote Sensing and Geographic Information System in Mineral Exploration," *Mineral Exploration*, edited by S. Haldar, Elsevier, Boston, 2013, pp. 95–115. https://doi.org/10.1016/b978-0-12-416005-7.00006-4.

[2] Benson, C. D., and Faherty, W. B., *Moonport: A history of Apollo launch facilities and operations*, Vol. 4204, Scientific and Technical Information Office, 1978. https://doi.org/10.2307/1855122.

[3] Modi, V. J., and Pande, K. C., "Magnetic-solar hybrid attitude control of satellites in near-equatorial orbits," *Journal of Spacecraft and Rockets*, Vol. 11, No. 12, 1974, pp. 845–851. https://doi.org/10.2514/3.27798.

[4] Goel, P., and Rajaram, S., "Magnetic attitude control of a momentum-biased satellite in near-equatorial orbit," *Journal of Guidance and Control*, Vol. 2, No. 4, 1979, pp. 334–338. https://doi.org//10.2514/3.55884.

[5] Shrivastava, S., and Modi, V., "Satellite attitude dynamics and control in the presence of environmental torques-A brief survey," *Journal of Guidance, Control, and Dynamics*, Vol. 6, No. 6, 1983, pp. 461–471. https://doi.org/10.2514/3.8526.

[6] Santoni, F., and Felicetti, L., "Attitude dynamics and control of drag-balance CubeSats," *Journal of Guidance, Control, and Dynamics*, Vol. 36, No. 6, 2013, pp. 1834–1839. https://doi.org/10.2514/1.59638.

[7] Pérez, D., and Bevilacqua, R., "Lyapunov-based adaptive feedback for spacecraft planar relative maneuvering via differential drag," *Journal of Guidance, Control, and Dynamics*, Vol. 37, No. 5, 2014, pp. 1678–1684. https://doi.org/10.2514/1.g000191.

[8] Groesbeck, D. S., Hart, K. A., and Gunter, B. C., "Simulated Formation Flight of Nanosatellites Using Differential Drag with High-Fidelity Rarefied Aerodynamics," *Journal of Guidance, Control, and Dynamics*, Vol. 42, No. 5, 2019, pp. 1175–1184. https://doi.org/10.2514/1.g003871.

[9] Hu, Y., Lu, Z., Liao, W., and Zhang, X., "Differential aerodynamic force-based formation control of nanosatellites using yaw angle deviation," *Journal of Guidance, Control, and Dynamics*, Vol. 44, No. 12, 2021, pp. 2199–2213. https://doi.org/10.2514/1.g006141.

[10] Omar, S. R., and Bevilacqua, R., "Spacecraft collision avoidance using aerodynamic drag," *Journal of Guidance, Control, and Dynamics*, Vol. 43, No. 3, 2020, pp. 567–573. https://doi.org/10.2514/1.g004518.

[11] Sun, R., Riano-Rios, C., Bevilacqua, R., Fitz-Coy, N. G., and Dixon, W. E., "Cubesat adaptive attitude control with uncertain drag coefficient and atmospheric density," *Journal of Guidance, Control, and Dynamics*, Vol. 44, No. 2, 2021, pp. 379–388. https://doi.org/10.2514/1.g005515.

[12] Berthet, M., and Suzuki, K., "Reverse Engineering of Perturbations in the Orbital Decay Environment from Nanosatellite Two-Line Elements," *Journal of Spacecraft and Rockets*, Vol. 59, No. 1, 2022, pp. 140–152. https://doi.org/10.2514/1.a34948.

[13] DeBra, D. B., "The effect of aerodynamic forces on satellite attitude," *J. Astronaut. Sci*, Vol. 6, No. 3, 1959, pp. 40–45.

[14] Beletskii, V. V., "Motion of an Artificial Satellite about its Center of Mass," *NASA TT F-429*, 1966.

[15] Meirovitch, L., and Wallace Jr, F., "On the effect of aerodynamic and gravitational torques on the attitude stability of satellites," *AIAA Journal*, Vol. 4, No. 12, 1966, pp. 2196–2202. https://doi.org/10.2514/3.3876.

[16] Frik, M. A., "Attitude stability of satellites subjected to gravity gradient and aerodynamic torques," *AIAA Journal*, Vol. 8, No. 10, 1970, pp. 1780–1785. https://doi.org/10.2514/6.1969-832.

[17] Psiaki, M. L., "Nanosatellite attitude stabilization using passive aerodynamics and active magnetic torquing," *Journal of Guidance, Control, and Dynamics*, Vol. 27, No. 3, 2004, pp. 347–355. https://doi.org/10.2514/1.1993.

[18] Morozov, V., and Kalenova, V., "Stabilization of Satellite Relative Equilibrium Using Magnetic Moments and Aerodynamic Forces," *Cosmic Research*, Vol. 60, No. 3, 2022, pp. 213–219. https://doi.org/10.1134/s0010952522030066.

[19] Chen, L., Gui, H., and Xiao, S., "Aerodynamic Attitude Control of Ultra-low Earth Orbit Satellite," *Advances in Guidance, Navigation and Control: Proceedings of 2022 International Conference on Guidance, Navigation and Control*, Springer, 2023, pp. 5898–5908. https://doi.org/10.1007/978-981-19-6613-2_570.

[20] Berthoud, L., Hills, R., Bacon, A., Havouzaris-Waller, M., Hayward, K., Gayrard, J.-D., Arnal, F., and Combelles, L., "Are Very Low Earth Orbit (VLEO) satellites a solution for tomorrow's telecommunication needs?" *CEAS Space Journal*, Vol. 14, No. 4, 2022, pp. 609–623. https://doi.org/10.1007/s12567-022-00437-0.

[21] Chen, G., Wu, S., Deng, Y., Jiao, J., and Zhang, Q., "VLEO Satellite Constellation Design for Regional Aviation and Marine Coverage," *IEEE Transactions on Network Science and Engineering*, 2023. https://doi.org/10.1109/globecom54140.2023.10437112.

[22] Luo, X., Chen, H.-H., and Guo, Q., "LEO/VLEO Satellite Communications in 6G and Beyond Networks–Technologies, Applications and Challenges," *IEEE Network*, 2024. https://doi.org/10.1109/mnet.2024.3353806.

[23] Herdrich, G., Papavramidis, K., Maier, P., Skalden, J., Hild, F., Beyer, J., Pfeiffer, M., Fugmann, M., Klinker, S., Fasoulas, S., et al., "System design study of a VLEO satellite platform using the IRS RF helicon-based plasma thruster," *Acta Astronautica*, Vol. 215, 2024, pp. 245–259. https://doi.org/10.1016/j.actaastro.2023.11.009.

[24] "QARMAN - QubeSat for Aerothermodynamic Research and Measurements on AblatioN," , 2023. URL https://www.vki.ac.be/index.php/qarman-home, accessed: 2022-06-21.

[25] Crisp, N. H., Roberts, P. C., Livadiotti, S., Rojas, A. M., Oiko, V., Edmondson, S., Haigh, S., Holmes, B., Sinpetru, L., Smith, K., et al., "In-orbit aerodynamic coefficient measurements using SOAR (Satellite for Orbital Aerodynamics Research)," *Acta Astronautica*, Vol. 180, 2021, pp. 85–99. https://doi.org/10.1016/j.actaastro.2020.12.024.

[26] Scala, F., Trisolini, M., Colombo, C., et al., "Attitude control of the disposal phase of the eCube mission for atmospheric data acquisition," *SpaceOps 2021 Virtual Edition*, 2021, pp. 1–17.

[27] Berthet, M., Yamada, K., Nagata, Y., and Suzuki, K., "Feasibility assessment of passive stabilisation for a nanosatellite with aeroshell deployed by orbit-attitude-aerodynamics simulation platform," *Acta Astronautica*, Vol. 173, 2020, pp. 266–278. https://doi.org/10.1016/j.actaastro.2020.04.043.

[28] Zuppardi, G., Savino, R., and Mongelluzzo, G., "Aero-thermo-dynamic analysis of a low ballistic coefficient deployable capsule in Earth re-entry," *Acta Astronautica*, Vol. 127, 2016, pp. 593–602. https://doi.org/10.1016/j.actaastro.2016.06.041.

[29] Saha, S. K., and Takahashi, Y., *Aero-structural Analysis of Deployable Aeroshell in Transonic Flow*, 2023. https://doi.org/10.2514/6.2023-2109, URL https://arc.aiaa.org/doi/abs/10.2514/6.2023-2109.

[30] Aslanov, V. S., and Sizov, D. A., "VLEO CubeSat attitude dynamics during and after flexible panels deployment using torsion springs," *Acta Astronautica*, 2023. https://doi.org/10.1016/j.actaastro.2023.05.011.

[31] Aslanov, V. S., "Chaotic attitude dynamics of a LEO satellite with flexible panels," *Acta Astronautica*, Vol. 180, 2021, pp. 538–544. https://doi.org/10.1016/j.actaastro.2020.12.055.

[32] Aslanov, V. S., and Sizov, D. A., "Chaos in flexible CubeSat attitude motion due to aerodynamic instability," *Acta Astronautica*, Vol. 189, No. May, 2021, pp. 310–320. https://doi.org/10.1016/j.actaastro.2021.08.055.

[33] Iñarrea, M., "Chaos and its control in the pitch motion of an asymmetric magnetic spacecraft in polar elliptic orbit," *Chaos, Solitons & Fractals*, Vol. 40, No. 4, 2009, pp. 1637–1652. https://doi.org/10.1016/j.chaos.2007.09.047.

[34] Liu, Y., and Chen, L., "Chaos in Spatial Attitude Motion of Spacecraft," *Chaos in Attitude Dynamics of Spacecraft*, Springer, 2013, pp. 99–129. https://doi.org/10.1007/978-3-642-30080-6_4.

[35] Aslanov, V. S., and Sizov, D. A., "Chaotic pitch motion of an aerodynamically stabilized magnetic satellite in polar orbits," *Chaos, Solitons & Fractals*, Vol. 164, 2022, p. 112718. https://doi.org/10.1016/j.chaos.2022.112718.

[36] Aslanov, V. S., and Sizov, D. A., "Attitude Dynamics of Spinning Magnetic LEO/VLEO Satellites," *Aerospace*, Vol. 10, No. 2, 2023, p. 192. https://doi.org/10.3390/aerospace10020192.

[37] Beletskii, V., and Grushevskii, A., "The evolution of the rotational motion of a satellite under the action of a dissipative aerodynamic moment," *Journal of Applied Mathematics and Mechanics*, Vol. 58, No. 1, 1994, pp. 11–19. https://doi.org/10.1016/0021-8928(94)90025-6.

[38] Boucher, D., "Non Complete integrability of a magnetic satellite in circular orbit," *Proceedings of the International Symposium on Symbolic and Algebraic Computation, ISSAC*, Vol. 2005, 2005, pp. 53–60. https://doi.org/10.1145/1073884.1073894.

[39] Maciejewski, A. J., and Przybylska, M., "Non-integrability of the problem of a rigid satellite in gravitational and magnetic fields," *Celestial Mechanics and Dynamical Astronomy*, Vol. 87, 2003, pp. 317–351. https://doi.org/10.1023/b:cele.0000006716.58713.ae.

[40] Curtis, H. D., *Orbital mechanics for engineering students*, Butterworth-Heinemann, 2013. https://doi.org/10.1016/b978-0-08-102133-0.00002-7.

[41] "International standard ISO 14222:2013. Space environment (natural and artificial) — Earth upper atmosphere," , 2013.

[42] Schrello, D., Davidson, P., and Juelich, O., "Passive Aerodynamic Attitude Stabilization of Near-Earth Satellites, Volume I. Librations Due to Combined Aerodynamic and Gravitational Torques," *North America Aviation Rept. WADD-TR-61-133, Columbus, OH*, 1961.

[43] Schaub, H., and Junkins, J. L., *Analytical mechanics of space systems*, AIAA, 2009. https://doi.org/10.2514/4.867231.

[44] Landau, L. D., and Lifshitz, E. M., *Course of theoretical physics. Volume 2: The classical theory of fields*, Elsevier, 2013.

[45] Goldstein, H., Poole, C., and Safko, J., "Classical mechanics," , 2002. https://doi.org/10.1119/1.1484149.

[46] Takahashi, Y., Ohashi, T., Oshima, N., Nagata, Y., and Yamada, K., "Aerodynamic instability of an inflatable aeroshell in suborbital re-entry," *Physics of fluids*, Vol. 32, No. 7, 2020. https://doi.org/10.1063/5.0009607.

[47] Schaaf, S., and Chambre, P., "Flow of Rarefied Gases, High Speed Aerodynamics and Jet Propulsion," *Fundamentals of Gas Dynamics*, Vol. 3, Princeton University Press NY, 1958. https://doi.org/10.1515/9781400877539-010.

[48] Carná, S. R., and Bevilacqua, R., "High fidelity model for the atmospheric re-entry of CubeSats equipped with the drag de-orbit device," *Acta Astronautica*, Vol. 156, 2019, pp. 134–156. https://doi.org/10.1016/j.actaastro.2018.05.049.